International Journal of Solids and Structures 130–131 (2018) 105–121

Contents lists available at ScienceDirect

International Journal of Solids and Structures

journal homepage: www.elsevier.com/locate/ijsolstr

Aspects of computational homogenization in magneto-mechanics: Boundary conditions, RVE size and microstructure composition

R. Zabihyan[a,*], J. Mergheim[a], A. Javili[b], P. Steinmann[a]

[a] Chair of Applied Mechanics, Universität Erlangen–Nürnberg, Egerlandstr. 5, Erlangen 91058, Germany
[b] Department of Mechanical Engineering, Bilkent University, Ankara 06800, Turkey

ARTICLE INFO

Article history:
Received 29 May 2017
Revised 26 September 2017
Available online 17 October 2017

Keywords:
Homogenization
Magneto-mechanics
Boundary condition

ABSTRACT

In the present work, the behavior of heterogeneous magnetorheological composites subjected to large deformations and external magnetic fields is studied. Computational homogenization is used to derive the macroscopic material response from the averaged response of the underlying microstructure. The microstructure consists of two materials and is far smaller than the characteristic length of the macroscopic problem. Different types of boundary conditions based on the primary variables of the magneto-elastic enthalpy and internal energy functionals are applied to solve the problem at the micro-scale. The overall responses of the RVEs with different sizes and particle distributions are studied under different loads and magnetic fields. The results indicate that the application of each set of boundary conditions presents different macroscopic responses. However, increasing the size of the RVE, solutions from different boundary conditions get closer to each other and converge to the response obtained from periodic boundary conditions.

1. Introduction

Magneto-active elastomers consist of a soft polymer matrix filled with magneto-active particles. They change their properties with the application of a magnetic field. The non-linear elastic characteristics of the matrix and the magnetic properties of the particles enable them to undergo very large and adjustable deformations in response to relatively low external magnetic fields. Due to such specifications these materials are of special interest for several engineering applications and attracted significant research attention (Kordonsky, 1993; Jolly et al., 1996; Carlson and Jolly, 2000).

The theoretical aspects of the magneto-mechanical response of solids have been thoroughly studied in the past. The general equations of magneto-elasticity and the solution of the resulting boundary value problems have been considered in the literature (Kovetz, 2000; Vu and Steinmann, 2007; Bustamante et al., 2008; Vu and Steinmann, 2010; Bustamante et al., 2011). In particular, the development of constitutive laws for magnetorheological elastomers are considered in Brigadnov and Dorfmann (2003), Kankanala and Triantafyllidis (2004), Steigmann (2004), Dorfmann and Ogden (2004) and Danas et al. (2012), among others, where the magnetorheological composites have been modeled on a macroscopic level. However, the strong dependency of the material response of the composites on their microstructure (e.g. shape, distribution, volume fraction and orientation of the particles) reveals the importance of multi-scale modeling techniques, where the macroscopic response is determined from the response of the material microstructure. Comprehensive reviews of various multi-scale modeling techniques are given in Saeb et al. (2016), Pindera et al. (2009) and Matous et al. (2017).

One of the most widely used multi-scale tools to predict the behavior of inhomogeneous materials is computational homogenization which is based on Hill (1963) and Hill and Rice (1972) and allows to study the effective behavior of composite materials (Kouznetsova et al., 2001; Miehe and Koch, 2002; Zohdi and Wriggers, 2001). The modeling of the behavior of composites based on computational homogenization in the context of the small strain as well as the finite strain setting has been studied extensively (Terada and Kikuchi, 1995; Ponte Castañeda, 1996; Terada and Kikuchi, 2001; Yvonnet et al., 2009; Miehe et al., 1999; Kouznetsova et al., 2002; Costanzo et al., 2005; Hirschberger et al., 2008; Temizer and Wriggers, 2008; Javili et al., 2013b), among others. Very recently, homogenization techniques have been utilized to study multiphysics problems. Extensions to coupled electro-mechanical response have been addressed in Schröder and Keip (2012), Kuznetsov and Fish (2012), Castañeda and Si-

* Corresponding author.
E-mail addresses: reza.zabihyan@ltm.uni-erlangen.de, reza.zabihyan@fau.de (R. Zabihyan), julia.mergheim@ltm.uni-erlangen.de (J. Mergheim), ajavili@bilkent.edu.tr (A. Javili), paul.steinmann@ltm.uni-erlangen.de (P. Steinmann).

https://doi.org/10.1016/j.ijsolstr.2017.10.009
0020-7683/

boni (2012) and Keip et al. (2014) and thermo-mechanical problems have been studied in Özdemir et al. (2008) and Temizer and Wriggers (2011). Moreover, magneto-mechanical homogenization of magnetorheological elastomers is considered in Borcea and Bruno (2001), Wang et al. (2003), Yin et al. (2006), Ponte Castañeda and Galipeau (2011) and Galipeau and Ponte Castañeda (2013). In the field of magneto-elasticity for finite deformations, Castañeda and Galipeau (2011), Ponte Castañeda and Galipeau (2011) and Galipeau and Ponte Castañeda (2013) introduced a finite-strain variational formulation where magnetoelastic effects are handled by means of the deformation-dependent magnetic susceptibility of the material. Danas (2017) proposed an augmented vector potential variational formulation to carry out numerical periodic homogenization studies on the magnetoelastic composites at finite strains and magnetic fields. Chatzigeorgiou et al. (2014) presented a general homogenization framework for magnetorheological elastomers under finite strains. They showed that the use of kinematic and magnetic field potentials, i.e. the variables of the enthalpy formulation, instead of kinetic field and magnetic induction potentials provides a more appropriate homogenization framework and convenient numerical implementation procedure. Based on this result, the numerical implementation of the homogenization procedure in finite strain magneto-mechanics is studied in Javili et al. (2013a) and Keip and Rambausek (2016). However, Miehe et al. (2016) showed that the computational framework based on the saddle-point-type magneto-elastic enthalpy functional is not advisable in order to detect instability points which occur in magnetorheological elastomers.[1] On the other hand, compared to the internal energy-based computational framework, the enthalpy-based formulation is very convenient for numerical implementation due to the reduction of the magnetic vector potential to a magnetic scalar potential . Therefore they proposed an internal energy-based computational homogenization framework based on scalar potentials by reformulation of the energy in terms of an averaged enthalpy functional. In the similar context, Gil and Ortigosa (2016) proposed a convex multi-variable framework for the analysis of the electro-active polymers undergoing large deformations and electric fields which satisfies material stability for the entire range of deformations and electric fields. These considerations of the internal energy density functional in terms of a convex multi-variable function of electromechanical arguments are inevitable in problems where the electro-mechanical enthalpy based formulation fails and yields non-physical material responses (Ortigosa and Gil, 2016b). Using the same analogy, the behavior of the incompressible electro-active polymers and electro-active shells undergoing large deformations and electric fields have been studied in Ortigosa et al. (2016) and Ortigosa and Gil. (2017). The extension of the variational convex multi-variable framework for the analysis of electro-magneto-mechanical internal energy functionals is carried on in Ortigosa and Gil (2016a) where the material stability of convex and non-convex multi-variable constitutive models is studied.

Central to computational homogenization is the Hill–Mandel condition which has to be satisfied by choosing appropriate boundary conditions for the microscopic problem. In the field of small strains Borcea and Bruno (2001) considered several types of boundary conditions and used prescribed displacements or tractions and an applied magnetic field at the boundary of the RVE. The application of a magnetic field as a boundary condition has also been considered in other micro-scale models together with boundary tractions (Yin et al., 2006) and strains (Yin et al., 2002). The homogenization of magnetostrictive particle-filled elastomers under periodic boundary conditions and constant magnetostrictive eigen-deformation in the ferromagnetic particles has been studied in Wang et al. (2003). Ponte Castañeda and Galipeau (2011) prescribed the deformation gradient tensor and the magnetic induction vector on the boundary of the microstructure and proposed a new homogenization framework for magneto-elastic composites which accounts for the effect of magnetic dipole interactions, as well as finite strains. Chatzigeorgiou et al. (2014) identified several cases of uniform boundary conditions on the RVE under which the Hill–Mandel condition holds.

The current contribution is an extension to the theory developed by Chatzigeorgiou et al. (2014). We numerically analyze the computational magneto-mechanical homogenization framework in the finite deformation setting with special focus on the two different sets of formulations based on the primary variables of the magneto-elastic enthalpy $W(\mathbf{F}, \mathbb{H})$ and the magneto-elastic internal energy $W^*(\mathbf{F}, \mathbb{B})$ functionals. For each set, we investigate several combinations of boundary conditions that satisfy the Hill–Mandel condition. Several numerical examples are given to study the microscopic and macroscopic responses of the RVEs with magneto-mechanical constituents which are different in sizes and particle distributions. Furthermore, the influence of the boundary conditions on the overall response of various microstructures, under different loads and magnetic fields, are studied and discussed in detail.

The structure of the paper is as follows. In Section 2, we describe the theoretical homogenization framework by presenting the field variables, the balance equations, the magneto-mechanical constitutive model that accounts for large deformations and the scale transition. Different sets of boundary conditions that satisfy the Hill–Mandel condition are described. In Section 3, the response of various composite materials which differ in particle size and distribution are studied under various magneto-mechanical loadings. Finally, Section 4 concludes this work.

2. Magneto-mechanical homogenization

The objective of this section is to summarize certain key concepts in the coupled magneto-mechanical homogenization framework and nonlinear continuum mechanics. Due to the inhomogeneous structure of composite materials, it is essential to consider separately micro and macro scales. The macro-scale describes the continuum body and the micro-scale describes the representative volume element (RVE) of the microstructure. As it is depicted in Fig. 1, both macro-scale and micro-scale can be expressed in the material or in the spatial configuration. In the current work we formulate the problem in the material description.

2.1. Micro-problem definition

In the undeformed configuration $\mathcal{B}_0$ at the micro-scale, the RVE occupies the volume V_0 with boundary $\partial\mathcal{B}_0$ (Fig. 1) and consists of two materials. In the deformed configuration $\mathcal{B}_t$ the RVE occupies the volume V_t with boundary $\partial\mathcal{B}_t$. The normal vectors to the boundaries $\partial\mathcal{B}_0$ and $\partial\mathcal{B}_t$ are denoted $\mathbf{N}$ and $\mathbf{n}$, respectively. The nonlinear deformation map $\mathbf{x} = \boldsymbol{\phi}(\mathbf{X})$ describes the position vector $\mathbf{x}$ of a point in the spatial configuration $\mathcal{B}_t$ in terms of the position vector $\mathbf{X}$ of the point in the material configuration $\mathcal{B}_0$. The microscopic deformation gradient $\mathbf{F}$ is connected to the deformation map $\boldsymbol{\phi}$ through the relation

$$\mathbf{F} = \nabla_{\mathbf{X}}\, \boldsymbol{\phi}\,. \tag{1}$$

[1] The stability analysis of the enthalpy based framework can be carried out using complex arc-length methods where the control variable is a combination of the magnetic potential and the magnetic field. See Belytschko et al. (2013) and Gil and Ortigosa (2016) for further details.

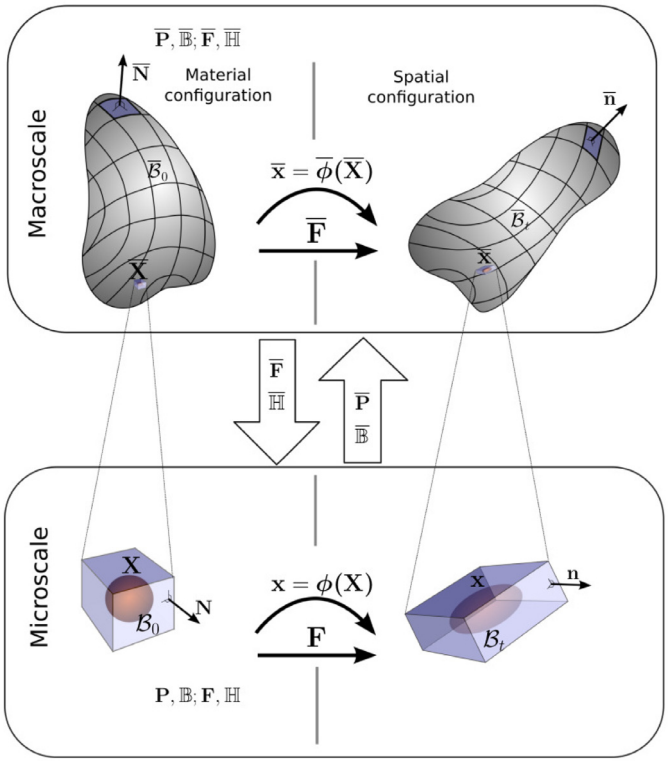

Fig. 1. Macro-scale and micro-scale in the material and the spatial configuration, enthalpy-based formulation.

In the absence of inertia and mechanical body forces at the micro-scale, the conservation of linear momentum reads

$$\text{Div}\ \mathbf{P} = \mathbf{0} \quad \text{in}\ \mathcal{B}_0\ . \tag{2}$$

where $\mathbf{P}$ is the Piola stress. It consists of the sum of the mechanical stress, the Maxwell stress and the stress due to material magnetization, see e.g. Steigmann (2004). The divergence operator with respect to the material coordinates $\mathbf{X}$ is denoted $\text{Div}\,\bullet$.

Ignoring any free current density at the micro-scale, the Lagrangian magnetic field $\mathbb{H}$ is connected with the scalar magnetic potential in the undeformed configuration $\varphi(\mathbf{X})$ through the relation

$$\mathbb{H} = \nabla_{\mathbf{X}}\, \varphi\,. \tag{3}$$

Moreover, the conservation of magnetic flux is written as

$$\text{Div}\ \mathbb{B} = 0 \quad \text{in}\ \mathcal{B}_0\,, \tag{4}$$

with the magnetic induction $\mathbb{B}$. The microscopic problem has to be completed by constitutive equations for the Piola stress $\mathbf{P}$ and the magnetic induction $\mathbb{B}$ and boundary conditions which follow from the scale-transition and will be discussed in detail in Section 2.3.

2.1.1. Microscopic magneto-mechanical constitutive model

With the help of magneto-elastic internal energy functionals, we can identify the constitutive relations that connect the Piola stress $\mathbf{P}$ and the magnetic induction $\mathbb{B}$ with the deformation gradient $\mathbf{F}$ and the magnetic field $\mathbb{H}$. Using the (saddle-point-type) magneto-elastic enthalpy function $W(\mathbf{F}, \mathbb{H})$ the Piola stress and the Lagrangian magnetic induction are given by

$$\mathbf{P} = \mathbf{P}(\mathbf{F}, \mathbb{H}) = \frac{\partial W(\mathbf{F}, \mathbb{H})}{\partial \mathbf{F}}\,, \qquad \mathbb{B} = \mathbb{B}(\mathbf{F}, \mathbb{H}) = -\frac{\partial W(\mathbf{F}, \mathbb{H})}{\partial \mathbb{H}}\,. \tag{5}$$

Using a Legendre transformation the magneto-elastic internal energy density function $W^*(\mathbf{F}, \mathbb{B})$, which is poly-convex in $\mathbf{F}$ when ($\mathbb{B} = 0$) and convex in the magnetic induction $\mathbb{B}$, see Gil and Ortigosa (2016), can be identified as

$$W^*(\mathbf{F}, \mathbb{B}) = \sup_{\mathbb{H}}\, [W(\mathbf{F}, \mathbb{H}) + \mathbb{B}\cdot\mathbb{H}]. \tag{6}$$

Furthermore, the constitutive relations for the Piola stress and the magnetic field can be derived based on the magneto-elastic internal energy density function $W^*(\mathbf{F}, \mathbb{B})$ as

$$\mathbf{P} = \mathbf{P}(\mathbf{F}, \mathbb{B}) = \frac{\partial W^*(\mathbf{F}, \mathbb{B})}{\partial \mathbf{F}}\,, \qquad \mathbb{H} = \mathbb{H}(\mathbf{F}, \mathbb{B}) = \frac{\partial W^*(\mathbf{F}, \mathbb{B})}{\partial \mathbb{B}}\,. \tag{7}$$

We assume an isotropic elastic material and an isotropic linear magnetic response for the matrix material and the magnetic particles, respectively. In order to establish appropriate constitutive relations and a convenient numerical implementation, the formulations are firstly derived in terms of a magneto-elastic enthalpy functional $W(\mathbf{F}, \mathbb{H})$, which for the sake of demonstration is here based on Neo-Hookean hyperelasticity, compare (Javili et al., 2013a)

$$W(\mathbf{F}, \mathbb{H}) = \frac{1}{2}\lambda_1[\mathbf{F}:\mathbf{F} - \mathit{Dim} - 2\ln \mathrm{J}\,] + \frac{1}{2}\lambda_2 \ln^2 \mathrm{J} - \frac{1}{2}\mu\,\mathrm{J}\,\mathbb{H}\cdot\mathbf{C}^{-1}\cdot\mathbb{H}\,, \tag{8}$$

where λ_1 and λ_2 are the Lamé parameters, μ is the magnetic permeability and *Dim* is the problem dimension. Also, $\mathbf{C} = \mathbf{F}^{\mathrm{t}}\cdot\mathbf{F}$ denotes the right Cauchy–Green deformation tensor and $\mathrm{J} = \det(\mathbf{F})$.[2] From the constitutive relation (5) the Piola stress $\mathbf{P}$ reads

$$\mathbf{P} = \frac{\partial W(\mathbf{F}, \mathbb{H})}{\partial \mathbf{F}} = \lambda_1\mathbf{F} + [\lambda_2 \ln \mathrm{J} - \lambda_1]\mathbf{F}^{-\mathrm{t}} - \frac{1}{2}\mu\,\mathrm{J}\,\mathbb{H}\otimes\mathbb{H} : \mathbf{M}\,, \tag{9}$$

with $\mathbf{M}$ defined as

$$\mathbf{M} := \mathbf{C}^{-1}\otimes\mathbf{F}^{-\mathrm{t}} + \frac{\partial \mathbf{C}^{-1}}{\partial \mathbf{F}}. \tag{10}$$

Furthermore, the magnetic induction $\mathbb{B}$ can be computed from (5) as

$$\mathbb{B} = -\frac{\partial W(\mathbf{F}, \mathbb{H})}{\partial \mathbb{H}} = \mu\,\mathrm{J}\,\mathbf{C}^{-1}\cdot\mathbb{H}\,. \tag{11}$$

As can be seen in Fig. 2(a) the enthalpy is a saddle-point-type function which does not permit in a straightforward manner the solution of stability problems or the derivation of bounds on the homogenized solution. A quasi-convex magneto-elastic internal energy density functional, which is also shown in Fig. 2(b), can be represented using Eq. (6) as

$$W^*(\mathbf{F}, \mathbb{B}) = \sup_{\mathbb{H}}[W(\mathbf{F}, \mathbb{H}) + \mathbb{B}\cdot\mathbb{H}] = \frac{1}{2}\lambda_1[\mathbf{F}:\mathbf{F} - \mathit{Dim} - 2\ln \mathrm{J}\,] + \frac{1}{2}\lambda_2 \ln^2 \mathrm{J} + \frac{1}{2}\frac{1}{\mu\,\mathrm{J}}\mathbb{B}\cdot\mathbf{C}\cdot\mathbb{B}. \tag{12}$$

From Eq. (7) the Piola stress $\mathbf{P}$ then reads

$$\mathbf{P} = \frac{\partial W^*(\mathbf{F}, \mathbb{B})}{\partial \mathbf{F}} = \lambda_1\mathbf{F} + [\lambda_2 \ln \mathrm{J} - \lambda_1]\mathbf{F}^{-\mathrm{t}} + \frac{1}{\mu\,\mathrm{J}}\mathbf{F}\cdot[\mathbb{B}\otimes\mathbb{B}] - \frac{1}{2\mu\,\mathrm{J}}[\mathbb{B}\cdot\mathbf{C}\cdot\mathbb{B}]\mathbf{F}^{-\mathrm{t}}. \tag{13}$$

Moreover, the magnetic field $\mathbb{H}$ is derived from (7) as

$$\mathbb{H} = \frac{\partial W^*(\mathbf{F}, \mathbb{B})}{\partial \mathbb{B}} = \frac{1}{\mu\,\mathrm{J}}\mathbf{C}\cdot\mathbb{B}. \tag{14}$$

Note that (9) and (13) as well as (11) and (14) are equivalent expressions, however in different parameterization.

[2] It should be mentioned that for very large volumetric strains the strain energy functional (8) does not fulfill the polyconvexity condition in $\mathbf{F}$ when ($\mathbb{H} = 0$), i.e. $\partial_{\mathrm{JJ}} W(\mathbf{F}) \geq 0$, see Doll and Schweizerhof (1999). However, in our study the volumetric strain is always small and therefore the polyconvexity condition is not violated.

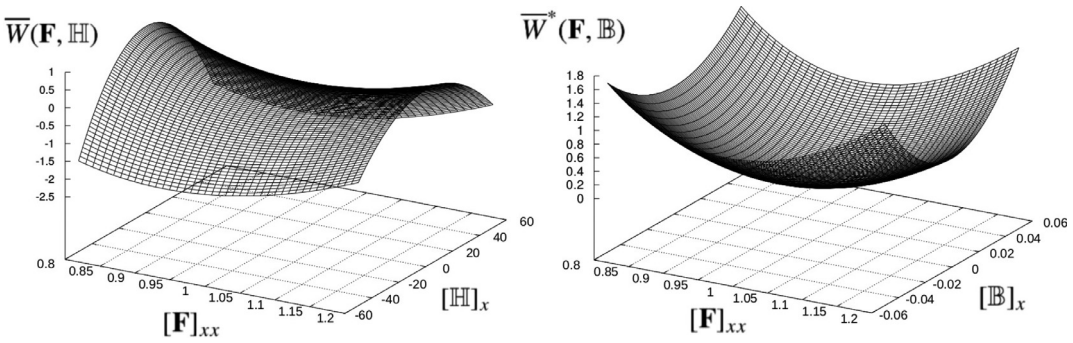

Fig. 2. Plots of (left) the macroscopic saddle-point magneto-elastic enthalpy $\overline{W}(\mathbf{F},\mathbb{H})$ and (right) the macroscopic magneto-elastic internal energy $\overline{W}^*(\mathbf{F},\mathbb{B})$ functionals with respect to $[\overline{\mathbf{F}}]_{xx}$, $[\overline{\mathbb{H}}]_x$ and $[\overline{\mathbf{B}}]_x$.

2.2. Macro-problem definition

A macroscopic continuum body occupies the material configuration $\overline{\mathcal{B}}_0$ with boundary $\partial\overline{\mathcal{B}}_0$ and the spatial configuration $\overline{\mathcal{B}}_t$ with boundary $\partial\overline{\mathcal{B}}_t$, see Fig. 1. For stationary applications, the macroscopic equilibrium equation in the material configuration is written as

$$\begin{aligned}&\overline{\text{Div}}\,\overline{\mathbf{P}}+\overline{\mathbf{b}}_0=\mathbf{0}\quad\text{in }\overline{\mathcal{B}_0}\quad\text{subject to}\quad\overline{\boldsymbol{\varphi}}=\overline{\boldsymbol{\varphi}}^p\quad\text{on }\partial\overline{\mathcal{B}_0}^{\mathcal{D}_{mech}}\text{ and}\\&[\![\overline{\mathbf{T}}]\!]=[\![\overline{\mathbf{P}}\cdot\overline{\mathbf{N}}]\!]=\overline{\mathbf{T}}^p\quad\text{on }\partial\overline{\mathcal{B}_0}^{\mathcal{N}_{mech}},\end{aligned}\tag{15}$$

with $\overline{\mathbf{b}}_0$ and $\overline{\mathbf{P}}$ are the macroscopic body force density and the macroscopic Piola stress in the material configuration, respectively. $\overline{\boldsymbol{\varphi}}$ and $\overline{\mathbf{T}}$ define the macroscopic deformation and tractions. Moreover, $\overline{\boldsymbol{\varphi}}^p$ is the prescribed deformation on the mechanical Dirichlet boundary and $\overline{\mathbf{T}}^p$ denotes the macroscopic prescribed tractions on the mechanical Neumann boundary, with $\partial\overline{\mathcal{B}_0}=\partial\overline{\mathcal{B}_0}^{\mathcal{D}_{mech}}\cup\partial\overline{\mathcal{B}_0}^{\mathcal{N}_{mech}}$ and $\partial\overline{\mathcal{B}_0}^{\mathcal{D}_{mech}}\cap\partial\overline{\mathcal{B}_0}^{\mathcal{N}_{mech}}=\emptyset$.
The conservation of the macroscopic magnetic flux is written

$$\begin{aligned}&\overline{\text{Div}}\,\overline{\mathbb{B}}=0\quad\text{in }\overline{\mathcal{B}_0}\quad\text{subject to}\quad\overline{\varphi}=\overline{\varphi}^p\quad\text{on }\partial\overline{\mathcal{B}_0}^{\mathcal{D}_{mag}}\text{ and}\\&[\![\overline{\mathbb{T}}]\!]=[\![\overline{\mathbb{B}}\cdot\overline{\mathbf{N}}]\!]=\overline{\mathbb{T}}^p\quad\text{on }\partial\overline{\mathcal{B}_0}^{\mathcal{N}_{mag}}.\end{aligned}\tag{16}$$

where $\overline{\mathbb{T}}^p$ is the prescribed macroscopic magnetic flux on the magnetic Neumann boundary $\partial\overline{\mathcal{B}_0}^{\mathcal{N}_{mag}}$. The macroscopic prescribed magnetic potential is described with $\overline{\varphi}^p$.

Due to the complex microstructure of composite materials, the constitutive relations between macroscopic stress, macroscopic deformation gradient, the macroscopic magnetic induction and macroscopic magnetic field are not explicitly expressed here, instead they are determined by means of computational homogenization i.e. using the solutions of the RVE problem at the micro-scale. The focus of the current work is on the microscopic response of the RVEs while studying the macro-scale solution is out of the scope of this paper. For complete two-scale solutions for magneto-active composites see e.g. Javili et al. (2013a),Keip and Rambausek (2016) and Sridhar et al. (2016).

2.3. Micro-to-macro transition

In order to establish a consistent transition between the micro- and macro-scale, the Hill–Mandel condition is required to be satisfied which stipulates the equivalence of the macroscopic variational enthalpy and the averaged microscopic variational enthalpy[3]

$$\begin{aligned}&\frac{1}{V_0}\int_{\mathcal{B}_0}\delta W\;\mathrm{d}V-\delta\overline{W}\\&\quad=\frac{1}{V_0}\int_{\mathcal{B}_0}[\mathbf{P}:\delta\mathbf{F}+\mathbb{B}\cdot\delta\mathbb{H}]\;\mathrm{d}V-[\overline{\mathbf{P}}:\delta\overline{\mathbf{F}}+\overline{\mathbb{B}}\cdot\delta\overline{\mathbb{H}}]=0\,.\end{aligned}\tag{17}$$

The mechanical and the magnetic terms of the Hill–Mandel condition can be separated as

$$\frac{1}{V_0}\int_{\mathcal{B}_0}\mathbf{P}:\delta\mathbf{F}\;\mathrm{d}V-\overline{\mathbf{P}}:\delta\overline{\mathbf{F}}=0,\tag{18a}$$

$$\frac{1}{V_0}\int_{\mathcal{B}_0}\mathbb{B}\cdot\delta\mathbb{H}\;\mathrm{d}V-\overline{\mathbb{B}}\cdot\delta\overline{\mathbb{H}}=0,\tag{18b}$$

respectively.

2.3.1. Mechanical average variables and boundary conditions

We assume that the microscopic motion $\boldsymbol{\varphi}$ is linked to the macroscopic deformation gradient by the standard first-order ansatz $\boldsymbol{\varphi}=\overline{\mathbf{F}}\cdot\mathbf{X}+\widetilde{\boldsymbol{\varphi}}(\mathbf{X})$, where $\widetilde{\boldsymbol{\varphi}}$ is the vector fluctuation field. Using Eq. (1) yields the microscopic deformation gradient $\mathbf{F}=\overline{\mathbf{F}}+\widetilde{\mathbf{F}}$, with the gradient of the fluctuations $\widetilde{\mathbf{F}}=\nabla_{\mathbf{X}}\widetilde{\boldsymbol{\varphi}}(\mathbf{X})$. Substituting this into (18a) results in

$$\left[\frac{1}{V_0}\int_{\mathcal{B}_0}\mathbf{P}\;\mathrm{d}V-\overline{\mathbf{P}}\right]:\delta\overline{\mathbf{F}}+\left[\frac{1}{V_0}\int_{\mathcal{B}_0}\mathbf{P}:\delta\widetilde{\mathbf{F}}\;\mathrm{d}V\right]=0\,.\tag{19}$$

The first term in Eq. (19) vanishes if the macroscopic Piola stress is equal to the volume average of its micro-scale counterpart, i. e.

$$\overline{\mathbf{P}}=\frac{1}{V_0}\int_{\mathcal{B}_0}\mathbf{P}\,\mathrm{d}V.\tag{20}$$

The second term in (19) is reformulated as a boundary integral

$$\begin{aligned}&\frac{1}{V_0}\int_{\mathcal{B}_0}\mathbf{P}:\delta\widetilde{\mathbf{F}}\;\mathrm{d}V=\frac{1}{V_0}\int_{\partial\mathcal{B}_0}\delta\widetilde{\boldsymbol{\varphi}}\cdot\mathbf{T}\,\mathrm{d}A=0\qquad\text{with}\\&\delta\widetilde{\boldsymbol{\varphi}}=\delta\boldsymbol{\varphi}-\overline{\mathbf{F}}\cdot\mathbf{X},\end{aligned}\tag{21}$$

and becomes zero by imposing one of the following constraints on the fluctuation field:

$$\begin{aligned}&\bullet\ \text{Voigt's assumption}&&\boldsymbol{\varphi}=\overline{\mathbf{F}}\cdot\mathbf{X}\quad\text{in }\mathcal{B}_0\,,\\&\bullet\ \text{Linear deformations}&&\boldsymbol{\varphi}=\overline{\mathbf{F}}\cdot\mathbf{X}\quad\text{on }\partial\mathcal{B}_0\\&\bullet\ \text{Periodic deformations}&&\widetilde{\boldsymbol{\varphi}}^+=\widetilde{\boldsymbol{\varphi}}^-\ \text{and}\\&\quad\text{anti-periodic tractions}&&\mathbf{T}^+=-\mathbf{T}^-\quad\text{on }\partial\mathcal{B}_0\,.\end{aligned}\tag{22}$$

The Neumann-type constraints can be derived by a priori assuming an additive decomposition of the Piola stress into macroscopic and fluctuating parts, $\mathbf{P}=\overline{\mathbf{P}}+\widetilde{\mathbf{P}}$. Substituting this result in (18a) gives

$$\frac{1}{V_0}\int_{\mathcal{B}_0}[\overline{\mathbf{P}}+\widetilde{\mathbf{P}}]:\delta\mathbf{F}\,\mathrm{d}V-\overline{\mathbf{P}}:\delta\overline{\mathbf{F}}=\overline{\mathbf{P}}:\left[\frac{1}{V_0}\int_{\mathcal{B}_0}\delta\mathbf{F}\,\mathrm{d}V-\delta\overline{\mathbf{F}}\right]$$

[3] The Hill–Mandel condition could also be formulated in form of the variational magneto-elastic internal energy density as $\delta W^*=\mathbf{F}:\delta\mathbf{P}+\mathbb{H}\cdot\delta\mathbb{B}$ which results in the same boundary conditions and is therefore not described.

$$+\frac{1}{V_0}\int_{\mathcal{B}_0}\widetilde{\mathbf{P}}:\delta\mathbf{F}\,\mathrm{d}V=0\,. \tag{23}$$

It follows that the macroscopic deformation gradient is the volume average of the microscopic deformation gradient

$$\overline{\mathbf{F}}=\frac{1}{V_0}\int_{\mathcal{B}_0}\mathbf{F}\,\mathrm{d}V, \tag{24}$$

and that the fluctuation term of the relation (23) should vanish. Using the divergence theorem and Eq. (2) yields the boundary integral

$$\begin{aligned}\frac{1}{V_0}\int_{\mathcal{B}_0}\widetilde{\mathbf{P}}:\delta\mathbf{F}\,\mathrm{d}V&=\frac{1}{V_0}\int_{\mathcal{B}_0}\mathrm{Div}(\delta\boldsymbol{\varphi}\cdot\widetilde{\mathbf{P}})\mathrm{d}V\\&=\frac{1}{V_0}\int_{\partial\mathcal{B}_0}\delta\boldsymbol{\varphi}\cdot\widetilde{\mathbf{P}}\cdot\mathbf{N}\,\mathrm{d}A=0.\end{aligned} \tag{25}$$

which vanishes if one of the following constraints is satisfied:

- Reuss' assumption $\quad\mathbf{P}=\overline{\mathbf{P}}\quad$ in $\mathcal{B}_0$. ,
- Constant tractions $\quad\mathbf{P}\cdot\mathbf{N}=\overline{\mathbf{P}}\cdot\mathbf{N}\quad$ on $\partial\mathcal{B}_0$ (26)

2.3.2. Magnetic average variables and boundary conditions

In a similar fashion to the mechanical problem, we assume a linear first-order ansatz for the microscopic magnetic potential, $\varphi=\overline{\mathbb{H}}\cdot\mathbf{X}+\widetilde{\varphi}(\mathbf{X})$, where $\widetilde{\varphi}$ is the scalar fluctuation field. Therefore, Eqs. (3) yields the microscopic magnetic field $\mathbb{H}=\overline{\mathbb{H}}+\widetilde{\mathbb{H}}$ with the fluctuation term $\widetilde{\mathbb{H}}=\nabla_{\mathbf{X}}\,\widetilde{\varphi}(\mathbf{X})$. Considering these equations and (18b) the Hill–Mandel condition can be written as

$$\left[\frac{1}{V_0}\int_{\mathcal{B}_0}\mathbb{B}\;\mathrm{d}V-\overline{\mathbb{B}}\right]\cdot\delta\overline{\mathbb{H}}+\left[\frac{1}{V_0}\int_{\mathcal{B}_0}\mathbb{B}\cdot\delta\widetilde{\mathbb{H}}\;\mathrm{d}V\right]=0\,, \tag{27}$$

whereby the first term vanishes if the macroscopic magnetic induction is equal to its averaged microscopic counterpart

$$\overline{\mathbb{B}}=\frac{1}{V_0}\int_{\mathcal{B}_0}\mathbb{B}\,\mathrm{d}V\;, \tag{28}$$

and the second term is formulated as a boundary integral

$$\begin{aligned}&\frac{1}{V_0}\int_{\mathcal{B}_0}\mathbb{B}\cdot\delta\widetilde{\mathbb{H}}\;\mathrm{d}V=\frac{1}{V_0}\int_{\partial\mathcal{B}_0}\delta\widetilde{\varphi}\cdot\mathbb{T}\,\mathrm{d}A=0\qquad\text{with}\\&\delta\widetilde{\varphi}=\delta\varphi-\overline{\mathbb{H}}\cdot\mathbf{X}.\end{aligned} \tag{29}$$

Eq. (29) can be satisfied by imposing one of the following constraints on the microscopic magnetic field:

- Voigt's assumption $\quad\varphi=\overline{\mathbb{H}}\cdot\mathbf{X}\quad$ in $\mathcal{B}_0$
- Linear magnetic potential $\quad\varphi=\overline{\mathbb{H}}\cdot\mathbf{X}\quad$ on $\partial\mathcal{B}_0$ (30)
- Periodic magnetic potential and anti-periodic magnetic flux $\quad\widetilde{\varphi}^{+}=\widetilde{\varphi}^{-}$ and $\mathbb{T}^{+}=-\mathbb{T}^{-}\quad$ on $\partial\mathcal{B}_0$.

The Neumann-type magnetic constraints can be obtained by a priori assuming an additive decomposition of the magnetic induction into macroscopic and fluctuating parts $\mathbb{B}=\overline{\mathbb{B}}+\widetilde{\mathbb{B}}$. Inserting this definition into (18b) gives

$$\begin{aligned}&\frac{1}{V_0}\int_{\mathcal{B}_0}[\overline{\mathbb{B}}+\widetilde{\mathbb{B}}]\cdot\delta\mathbb{H}\,\mathrm{d}V-\overline{\mathbb{B}}\cdot\delta\overline{\mathbb{H}}=\overline{\mathbb{B}}\cdot\left[\frac{1}{V_0}\int_{\mathcal{B}_0}\delta\mathbb{H}\,\mathrm{d}V-\delta\overline{\mathbb{H}}\right]\\&+\frac{1}{V_0}\int_{\mathcal{B}_0}\widetilde{\mathbb{B}}\cdot\delta\mathbb{H}\,\mathrm{d}V=0\,.\end{aligned} \tag{31}$$

Satisfaction of the Hill–Mandel condition requires that the macroscopic magnetic field is the volume average of the microscopic magnetic field

$$\overline{\mathbb{H}}=\frac{1}{V_0}\int_{\mathcal{B}_0}\mathbb{H}\,\mathrm{d}V\;, \tag{32}$$

and that the fluctuation term of the relation (31) should vanish. Using the divergence theorem and Eq. (4) yields a boundary integral

$$\begin{aligned}\frac{1}{V_0}\int_{\mathcal{B}_0}\widetilde{\mathbb{B}}\cdot\delta\mathbb{H}\,\mathrm{d}V&=\frac{1}{V_0}\int_{\mathcal{B}_0}\mathrm{Div}(\delta\varphi\cdot\widetilde{\mathbb{B}})\mathrm{d}V\\&=\frac{1}{V_0}\int_{\partial\mathcal{B}_0}\delta\varphi\cdot\widetilde{\mathbb{B}}\cdot\mathbf{N}\,\mathrm{d}A=0\;,\end{aligned} \tag{33}$$

which becomes zero on the boundary $\partial\mathcal{B}_0$ if one of the following constraints is satisfied:

- Reuss' assumption $\quad\mathbb{B}=\overline{\mathbb{B}}\quad$ in $\mathcal{B}_0$,
- Constant magnetic induction $\quad\mathbb{B}\cdot\mathbf{N}=\overline{\mathbb{B}}\cdot\mathbf{N}\quad$ on $\partial\mathcal{B}_0$. (34)

Table 1 summarizes different combinations of the boundary conditions, derived in Eqs. (22), (26), (30), (34). The first set is based on the primary variables of the magneto-elastic enthalpy functional $W(\mathbf{F},\mathbb{H})$. This formulation results in a saddle-point problem which is not straightforward to perform a classical stability analysis and also is not capable of tracking postcritical solution paths associated with instabilities. Therefore, stability analysis should be based on the energetic formulation (Miehe et al., 2016). The second group of boundary conditions in Table 1 are based on the primary variables of the magneto-elastic internal energy functional $W^{*}(\mathbf{F},\mathbb{B})$.

Remark: Note that the Voigt's and Reuss' assumptions based on prescribed deformation gradient $\overline{\mathbf{F}}$ and magnetic field $\overline{\mathbb{H}}$ are different from the Voigt* and Reuss* assumptions based on variables of the internal energy function -prescribed deformation gradient $\overline{\mathbf{F}}$ and magnetic induction $\overline{\mathbb{B}}$- and they shall not be mistaken.

The numerical implementation of the microscopic problem based on the finite element method and the algorithms to prescribe the various boundary conditions are described in Appendix A.

3. Numerical examples

The objective of this section is to present numerical examples in order to study the influence of different microstructures, boundary conditions and RVE sizes on the macroscopic response of magneto-mechanical composites. The composites are considered in a plane-strain setting and consist of a matrix material and circular inclusions. In the following numerical examples the material parameters of the matrix are assumed to be: Lamé parameters $\lambda_1^{mat.}=8$, $\lambda_2^{mat.}=12$, magnetic permeability $\mu^{mat.}=0.001$, and the material parameters of the inclusion are: Lamé parameters $\lambda_1^{inc.}=80$, $\lambda_2^{inc.}=120$ and magnetic permeability $\mu^{inc.}=0.01$. Simple-extension and simple shear loads are prescribed by imposing the deformation gradient in x-direction or in the xy-plane,

$$\overline{\mathbf{F}}=\begin{bmatrix}[\overline{\mathbf{F}}]_{xx}&0\\0&1\end{bmatrix},\qquad\overline{\mathbf{F}}=\begin{bmatrix}1&[\overline{\mathbf{F}}]_{xy}\\0&1\end{bmatrix}.$$

Furthermore, a magnetic loading is applied by imposing either the magnetic field or the magnetic induction in x-direction

$$\overline{\mathbb{H}}=\begin{bmatrix}[\overline{\mathbb{H}}]_x\\0\end{bmatrix},\qquad\overline{\mathbb{B}}=\begin{bmatrix}[\overline{\mathbb{B}}]_x\\0\end{bmatrix}.$$

All examples are solved using our in-house finite element code and are discretized with bilinear quadrilateral Q_1 elements. The solution procedure is robust and shows for all examples asymptotically the quadratic rate of convergence associated with the Newton-Raphson scheme.

3.1. Unit cell under magnetic field, stretching and shearing

The aim of this first example is to demonstrate the influence of different boundary conditions on the effective and the microscopic response of the RVE. A composite consisting of a matrix material and periodically aligned inclusions is represented by means of the two-dimensional unit cell illustrated in Fig. 3.

Fig. 4 shows the distributions of the microscopic normalized Piola stress and the microscopic normalized magnetic induction

Table 1
Conditions for satisfying the Hill–Mandel condition.

Constraint	Conditions based on prescribed ($\overline{\mathbf{F}}$, $\overline{\mathbb{H}}$)					
Voigt	Lin. displacement:	$\boldsymbol{\phi} = \overline{\mathbf{F}} \cdot \mathbf{X}$	Lin. magnetic potential:	$\varphi = \overline{\mathbb{H}} \cdot \mathbf{X}$	in $\mathcal{B}_0$	
LD-LP	Lin. displacement:	$\boldsymbol{\phi} = \overline{\mathbf{F}} \cdot \mathbf{X}$	Lin. magnetic potential:	$\varphi = \overline{\mathbb{H}} \cdot \mathbf{X}$	on $\partial\mathcal{B}_0$	Alg. 1
PD-PP	Per. displacements:	$\widetilde{\boldsymbol{\phi}}^{+} = \widetilde{\boldsymbol{\phi}}^{-}$	Per. magnetic potential:	$\widetilde{\varphi}^{+} = \widetilde{\varphi}^{-}$	on $\partial\mathcal{B}_0$	Alg. 2
CT-CI	Const. traction:	$\mathbf{P} \cdot \mathbf{N} = \overline{\mathbf{P}} \cdot \mathbf{N}$	Const. magnetic induction:	$\mathbb{B} \cdot \mathbf{N} = \overline{\mathbb{B}} \cdot \mathbf{N}$	on $\partial\mathcal{B}_0$	Alg. 3
Reuss	Const. traction:	$\mathbf{P} = \overline{\mathbf{P}}$	Const. magnetic induction:	$\mathbb{B} = \overline{\mathbb{B}}$	in $\mathcal{B}_0$	
Constraint	Conditions based on prescribed ($\overline{\mathbf{F}}$, $\overline{\mathbb{B}}$)					
Voigt*	Lin. displacement:	$\boldsymbol{\phi} = \overline{\mathbf{F}} \cdot \mathbf{X}$	Const. magnetic induction:	$\mathbb{B} = \overline{\mathbb{B}}$	in $\mathcal{B}_0$	
LD-CI	Lin. displacement:	$\boldsymbol{\phi} = \overline{\mathbf{F}} \cdot \mathbf{X}$	Const. magnetic induction:	$\mathbb{B} \cdot \mathbf{N} = \overline{\mathbb{B}} \cdot \mathbf{N}$	on $\partial\mathcal{B}_0$	Alg. 4
PD-PP	Per. displacements:	$\widetilde{\boldsymbol{\phi}}^{+} = \widetilde{\boldsymbol{\phi}}^{-}$	Per. magnetic potential:	$\widetilde{\varphi}^{+} = \widetilde{\varphi}^{-}$	on $\partial\mathcal{B}_0$	Alg. 5
CT-LP	Const. traction:	$\mathbf{P} \cdot \mathbf{N} = \overline{\mathbf{P}} \cdot \mathbf{N}$	Lin. magnetic potential:	$\varphi = \overline{\mathbb{H}} \cdot \mathbf{X}$	on $\partial\mathcal{B}_0$	Alg. 6
Reuss*	Const. traction:	$\mathbf{P} = \overline{\mathbf{P}}$	Lin. magnetic potential:	$\varphi = \overline{\mathbb{H}} \cdot \mathbf{X}$	in $\mathcal{B}_0$	

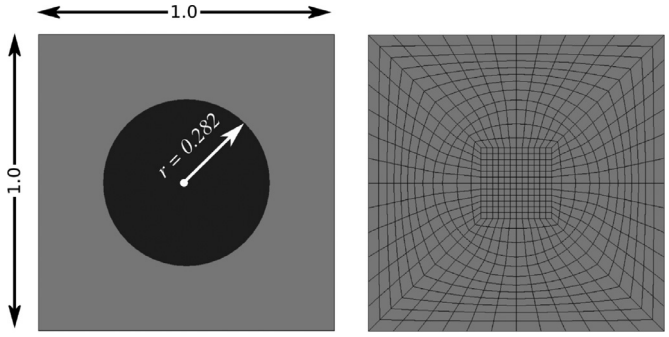

Fig. 3. Unit cell of a fiber composite and the associated finite element discretization. The volume fraction of the inclusion fiber is $f = 25\%$.

in the unit-cell microctructure which undergoes 10% of simple-stretch in x-direction $[\overline{\mathbf{F}}]_{xx} = 1.1$ and a magnetic field in x-direction $[\overline{\mathbb{H}}]_x = 50$. It can be observed that the three different boundary conditions result in very similar homogenized stresses and magnetic inductions. The maximum difference between them is below 2%. The microscopic answers are also similar, although the CT-CI boundary conditions result in slightly lower maximal stress and induction values.

In the next example, the same unit cell is subject to 10% of simple-shear deformation in the xy-plane $[\overline{\mathbf{F}}]_{xy} = 0.1$ and a magnetic field in the x-direction $[\overline{\mathbb{H}}]_x = 50$. The distributions of the microscopic shear stress, normalized by its macroscopic counterpart, and the microscopic magnetic induction in the x-direction, normalized by the macroscopic magnetic induction, are presented in Fig. 5. It is again found that the homogenized stresses and magnetic inductions are very similar for all three boundary conditions. However, the macroscopic magnetic inductions are approximately 16% higher than in the previous simple-extension example. This is due to the magneto-mechanical coupling effect in simple-extension. The distances between the particles increase and therefore the homogenized magnetic permeability decreases. The microscopic distributions of the stresses and the magnetic inductions and their maximum values show small differences for the three different boundary condition. The highest microscopic stress and induction values are obtained for the LD-LP boundary conditions. The influence of the different boundary conditions on the homog-

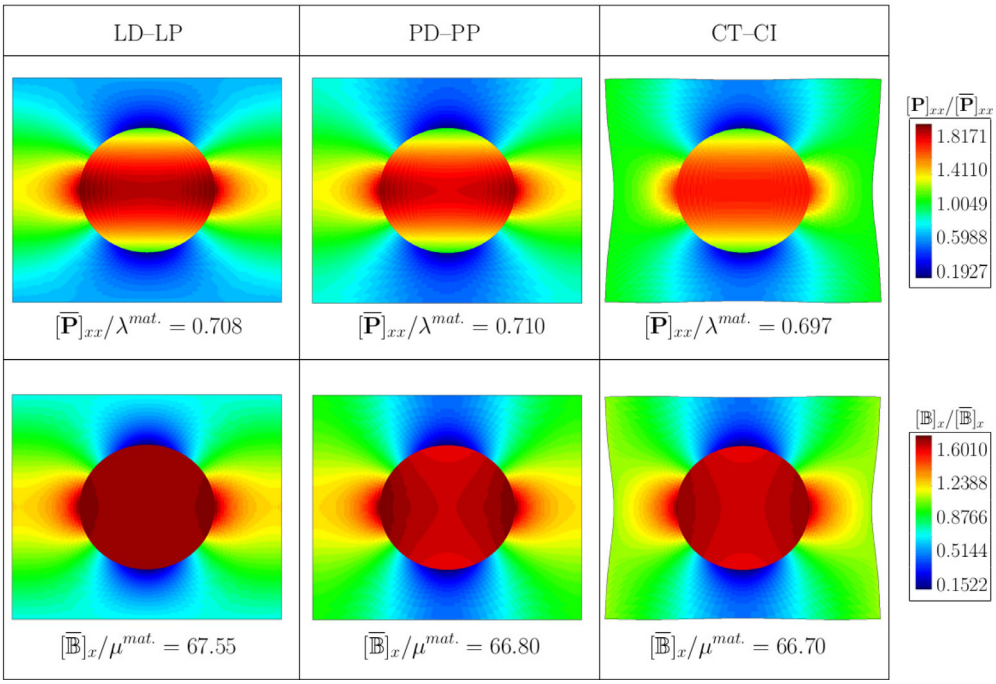

Fig. 4. Macroscopic stretching $[\overline{\mathbf{F}}]_{xx} = 1.1$ and magnetic field $[\overline{\mathbb{H}}]_x = 50$: distribution of microscopic normalized Piola stress (xx-component) and normalized magnetic induction in x-direction for applied LD-LP, PD-PP and CT-CI boundary conditions.

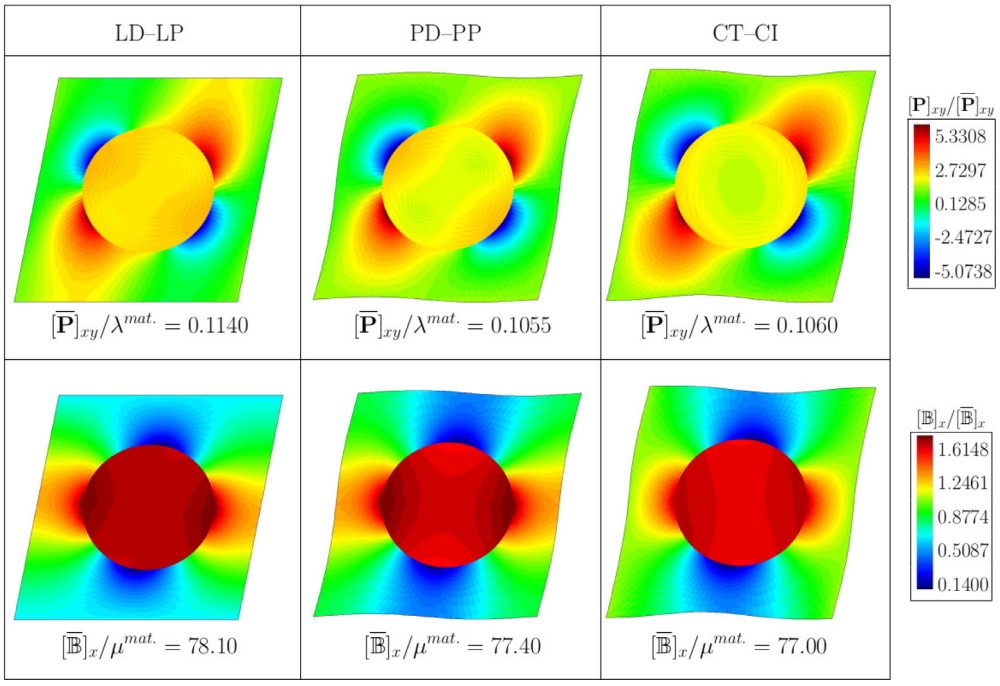

Fig. 5. Macroscopic shearing $[\overline{\mathbf{F}}]_{xy} = 0.1$ and magnetic field $[\overline{\mathbb{H}}]_x = 50$: distribution of microscopic normalized Piola stress (xy-component) and normalized magnetic induction in x-direction for applied LD-LP, PD-PP and CT-CI boundary conditions.

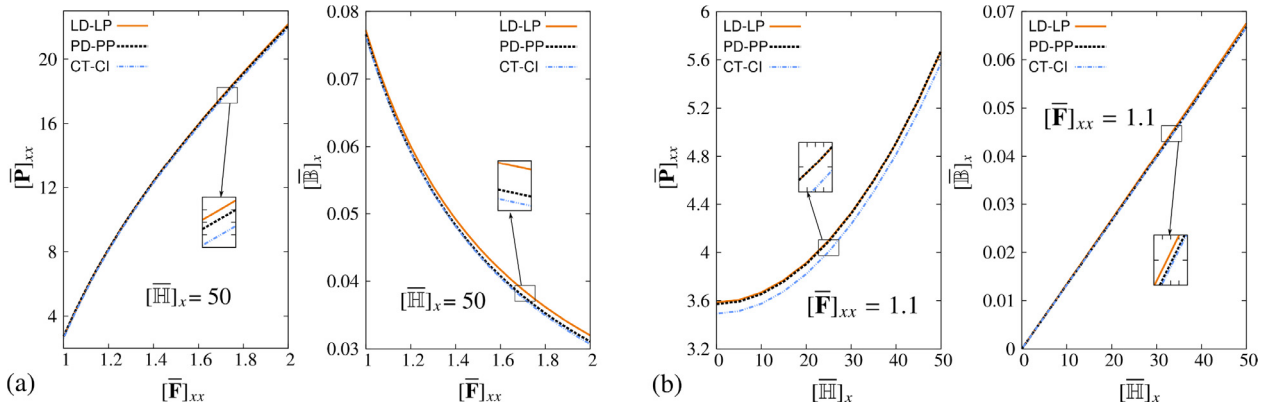

Fig. 6. Variations of the (a) macroscopic Piola stress (xx-component) and macroscopic magnetic induction (in x-direction) due to the increase of the stretch for the simple-extension under magnetic field $[\overline{\mathbb{H}}]_x = 50$ and (b) macroscopic Piola stress (xx-component) and magnetic induction (in x-direction) due to the increase of the magnetic field under simple-extension $[\overline{\mathbf{F}}]_{xx} = 1.1$ load, for applied LD-LP, PD-PP and CT-CI boundary conditions.

enized stress and magnetic induction is not very high in this unit cell example, however the differences in the microscopic fields and their maximum values are more pronounced.

Fig. 6 compares the graphs of the macroscopic macroscopic Piola stress (xx-component) and macroscopic magnetic induction (in x-direction) obtained from the increase of the stretch $[\overline{\mathbf{F}}]_{xx}$ for the simple-extension and magnetic field $[\overline{\mathbb{H}}]_x$. It can be observed that, also under increasing mechanical and magnetic loads, the three different boundary conditions result in very similar homogenized stresses and magnetic inductions. The highest difference belongs to the variation of the macroscopic Piola stress versus the magnetic field, where the CT-CI b.c. underestimates the results obtained from the other boundary conditions, Fig. 6 b (left).

3.2. Periodic, random mono-disperse and poly-disperse microstructures under magnetic field, stretching and shearing

In this section the microscopic behavior of three different microstructures, periodic, random mono-disperse and random poly-disperse, compare Fig. 7, is analyzed. The volume fraction of all microstructures is 25% and periodic (PD-PP) boundary conditions are applied.

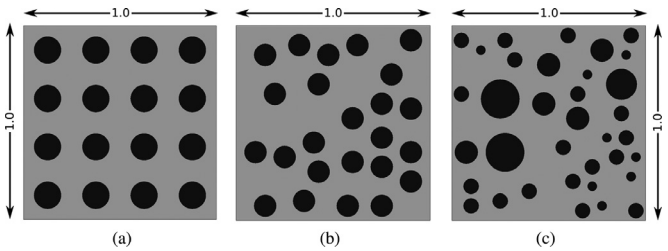

Fig. 7. Three different (a) periodic, (b) random mono-disperse and (c) random poly-disperse RVEs with the same volume fraction of $f = 25\%$.

Fig. 8 shows the obtained microscopic Piola stress and the magnetic induction in x-direction, normalized by their macroscopic counterparts, for the RVEs that undergo 10% of simple-extension

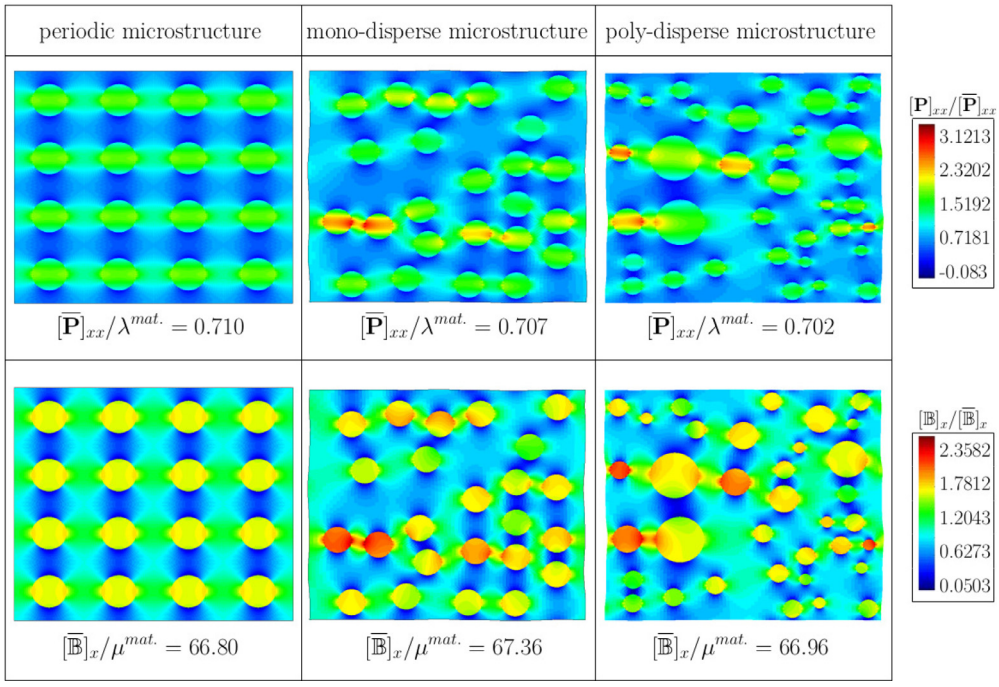

Fig. 8. Macroscopic stretching $[\overline{\mathbf{F}}]_{xx} = 1.1$ and magnetic field $[\overline{\mathbb{H}}]_x = 50$: distribution of microscopic normalized Piola stress (*xx*-component) and normalized magnetic induction in *x*-direction for different periodic, random mono-disperse and random poly-disperse microstructures.

deformation and a magnetic field of $[\overline{\mathbb{H}}]_x = 50$. The homogenized values for the Piola stress and the magnetic induction are very similar for all three microstructures and differ at most by 2%. However, the microscopic distributions of stress and induction show large variations: the periodic microstructure represents a more uniform distribution of the microscopic quantities, whereas the random mono-disperse and random poly-disperse RVEs show quite different microscopic responses.

It can be observed that the proximity of particles aligned in the direction of the applied magnetic field and also the existence of a small particle in the vicinity of a bigger one, lead to higher values of the microscopic magnetic induction and consequently to higher microscopic stresses. The maximum stress values in the random RVEs are two times higher than the maximum stress in the periodic microstructure.

Fig. 9 presents the distributions of the microscopic shear stress and the microscopic magnetic induction in x direction, normalized by their macroscopic counterparts. The RVEs are loaded by 10% of simple-shear deformation in the xy-plane, $[\overline{\mathbf{F}}]_{xy} = 0.1$ and a magnetic field in *x*-direction, $[\overline{\mathbb{H}}]_x = 50$.

The homogenized Piola stresses and magnetic inductions are again very similar for all three microstructures. The macroscopic induction is for all RVEs higher than in the previous example with simple-extension although the same magnetic field is applied. The reason is the same as in the unit cell example: The distances between the particles are increased in simple-extension and therefore the homogenized magnetic permeability decreases. The microscopic distributions of the shear stress and the magnetic inductions differ significantly: the maximum magnetic induction in the periodic microstructure is half of that in the random microstructures. The normalized microscopic shear stress in the periodic microstructure ranges from −4.90 to 5.17 whereas the random mono-disperse microstructure shows normalized shear stresses between −12.37 and 11.83. The decisive factor for the magnitude of the microscopic induction and consequently also for the magnitude of the stress is the distance between two particles in the direction of the magnetic field. Therefore, high magnetic induction and stress values are obtained for the random microstructures at certain points, which are canceled out during homogenization but are crucial for the microscopic behavior of the material.

The curves of homogenized Piola stress and magnetic induction for the periodic, mono-disperse and poly-disperse microstructures obtained from PD-PP b.c. are compared in Fig. 10. The numerical results prove that the homogenized Piola stresses and magnetic inductions are very similar for the three different microstructures.

It can be summarized, that the microscopic material behavior of a magneto-active composite strongly depends on the distribution of the particles. The macroscopic material behavior, e.g. the homogenized stresses, strains or magnetic fields observed in an experiment, might be similar for various microstructures, but the microscopic loading can be significantly different depending on the minimum distances of particles. Considering the modeling and simulation of magneto-active materials, it seems to be very important to represent the microstructures as accurately as possible to compute the correct maximum values of stresses and magnetic inductions on the micro-scale. If one is mainly interested in the homogenized material answer a periodic unit cell gives sufficiently accurate results.

3.3. Convergence of homogenized variables for different boundary conditions

The objective of this section is to compare the numerical results obtained from the application of different boundary conditions for increasing sizes of the RVEs. Fig. 11 (a) and (b) illustrates multiple sizes of periodic and random poly-disperse RVEs. Note that their size increases in such a way that the higher level includes the underlying lower levels. The response of the random microstructure of a particular size is obtained by solving and averaging ten different poly-disperse RVEs. Fig. 11(c) shows an example of those ten samples for the size 1x1. In the first step the same boundary conditions as in the previous unit cell example are applied, i.e. depending on the primary variables of the magneto-elastic enthalpy

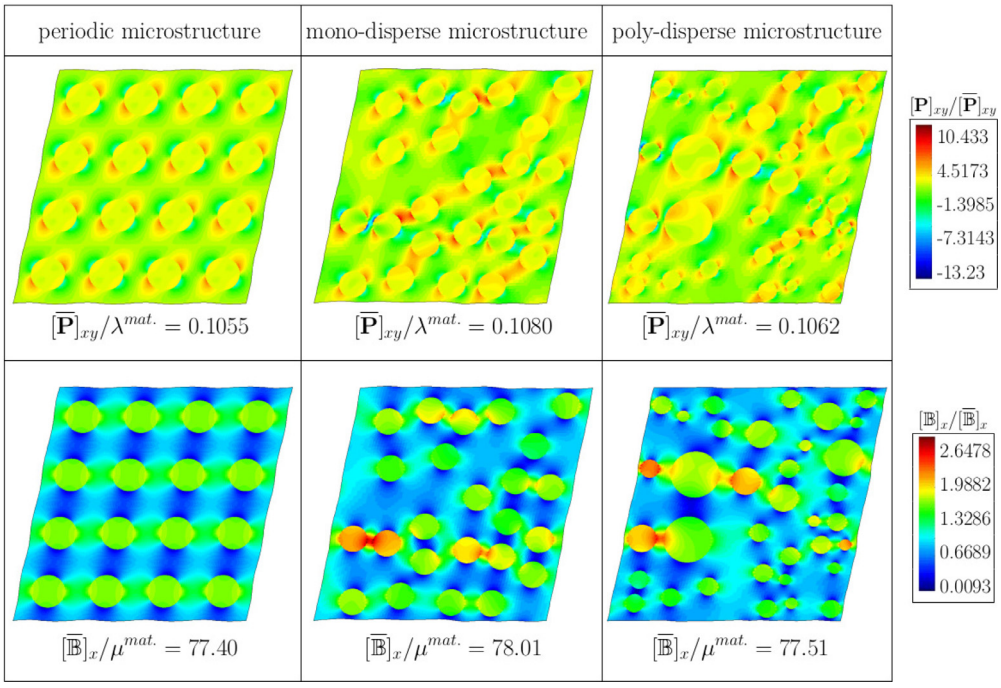

Fig. 9. Macroscopic shearing $[\overline{\mathbf{F}}]_{xy} = 0.1$ and magnetic field $[\overline{\mathbb{H}}]_x = 50$: distribution of microscopic normalized Piola stress (xy-component) and normalized magnetic induction in x-direction for different periodic, random mono-disperse and random poly-disperse microstructures.

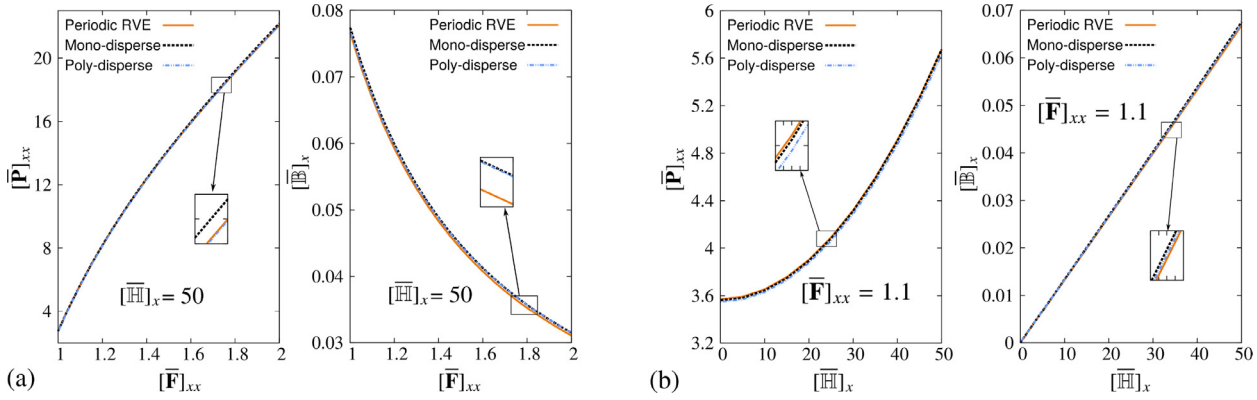

Fig. 10. Variations of the (a) macroscopic Piola stress (xx-component) and macroscopic magnetic induction (in x-direction) due to the increase of the stretch for the simple-extension under magnetic field $[\overline{\mathbb{H}}]_x = 50$ and (b) macroscopic Piola stress (xx-component) and magnetic induction (in x-direction) due to the increase of the magnetic field under simple-extension $[\overline{\mathbf{F}}]_{xx} = 1.1$ load, for periodic, mono-disperse and poly-disperse RVEs.

function $W(\mathbf{F}, \mathbb{H})$. Secondly, boundary conditions are prescribed in terms of the primary variables of the magneto-elastic internal energy function $W^*(\mathbf{F}, \mathbb{B})$.

3.3.1. Boundary conditions based on primary variables of enthalpy function $W(\mathbf{F}, \mathbb{H})$

Fig. 12 illustrates the variation of macroscopic quantities, i.e. the enthalpy $\overline{W}$, the Piola stress $[\overline{\mathbf{P}}]_{xx}$ and the magnetic induction $[\overline{\mathbb{B}}]_x$, versus the size of a periodic RVE. The microstructures are subject to two different load cases, one with simple-extension $[\overline{\mathbf{F}}]_{xx} = 1.1$ and a magnetic field $[\overline{\mathbb{H}}]_x = 7.6$ in x-direction and the second one with no deformation $[\overline{\mathbf{F}}] = \mathbb{I}$ and a magnetic field $[\overline{\mathbb{H}}]_x = 6.6$ in x-direction. The top row of Fig. 12 shows the numerical results obtained for the first load case, the bottom row those for the second load case.

In the top row of Fig. 12, it is firstly observed that the results of all boundary conditions converge to the results of the periodic boundary conditions, as expected. The LD-LP boundary conditions render higher averaged quantities than the PD-PP boundary conditions, and the CT-CI boundary conditions result in lower averaged values. The results converge for increasing sizes of the RVEs at different rates for the various boundary conditions. For the magneto-elastic enthalpy and the stress, the LD-LP boundary conditions converge much faster than the CT-CI boundary conditions. In contrast, for the magnetic induction, the CT-CI boundary conditions show a slightly faster convergence. The Voigt's approximation gives the highest results in all three cases, the Reuss' approximation the lowest one. The second load case, i.e. with a prescribed deformation gradient of $[\overline{\mathbf{F}}] = \mathbb{I}$, is considered in the bottom row of Fig. 12. The results for all boundary conditions also converge to the results of the periodic boundary conditions for increasing sizes of the RVEs. However, some differences in the order of the results can be observed. The homogenized magneto-elastic enthalpy, computed with the LD-LP boundary conditions is always smaller than the result of the PD-PP boundary conditions, and the magneto-elastic enthalpy derived with the CT-CI boundary conditions is always higher. The Voigt's and Reuss' approximations show a similar behavior, i.e. Voigt's approximation renders a smaller enthalpy

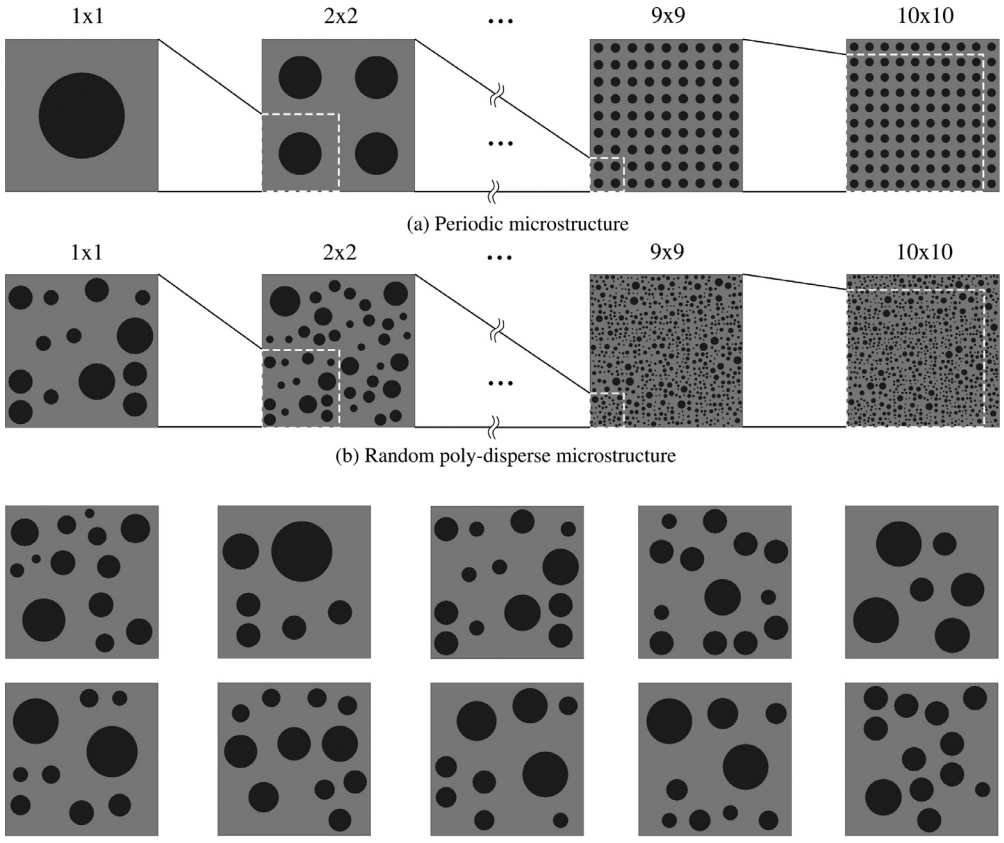

Fig. 11. Different sizes (levels) of (a) periodic and (b) random poly-disperse microstructures with the same volume fraction of $f = 25\%$. The size increases in such a way that the higher level includes the underlying lower levels and the volume fraction remains constant.(c) shows ten random poly-disperse RVE of size 1x1.

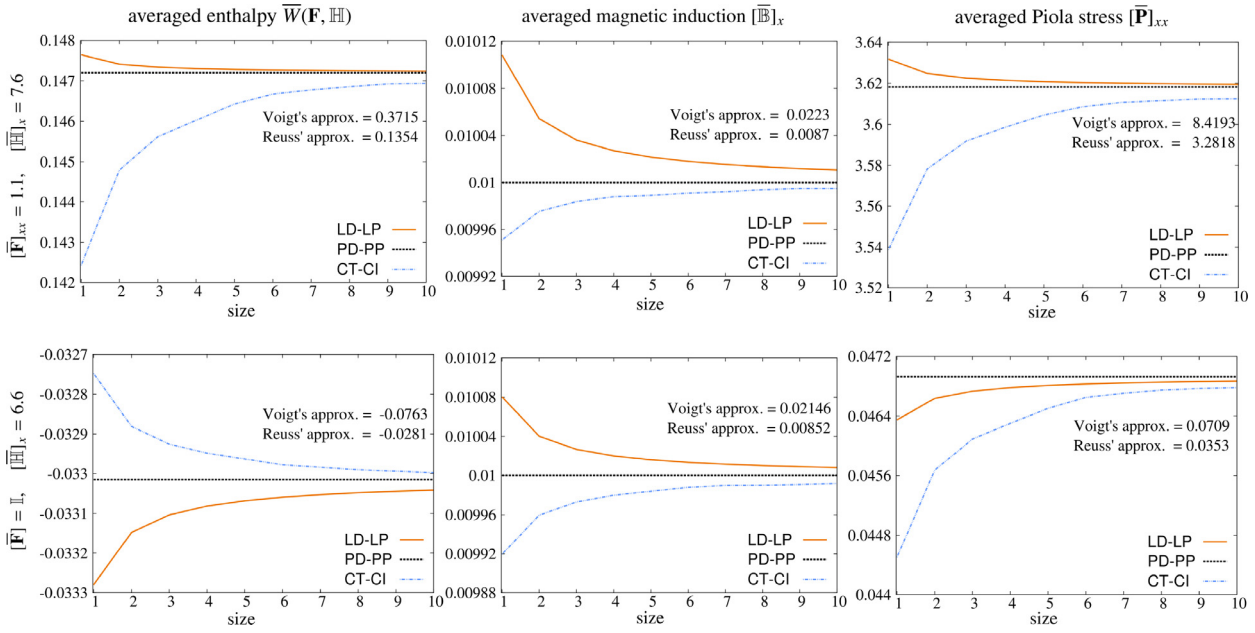

Fig. 12. Comparison of the macroscopic enthalpy $\overline{W}$, macroscopic magnetic induction $[\overline{\mathbb{B}}]_x$ and macroscopic Piola stress $[\overline{\mathbf{P}}]_{xx}$, obtained from the application of LD-LP, PD-PP, CT-CI b.cs. and Voigt's and Reuss' approximation to the periodic microstructures. The size of the RVE increases from a unit-cell to a 10x10 periodic microstructure that contains all underlying lower size RVEs.

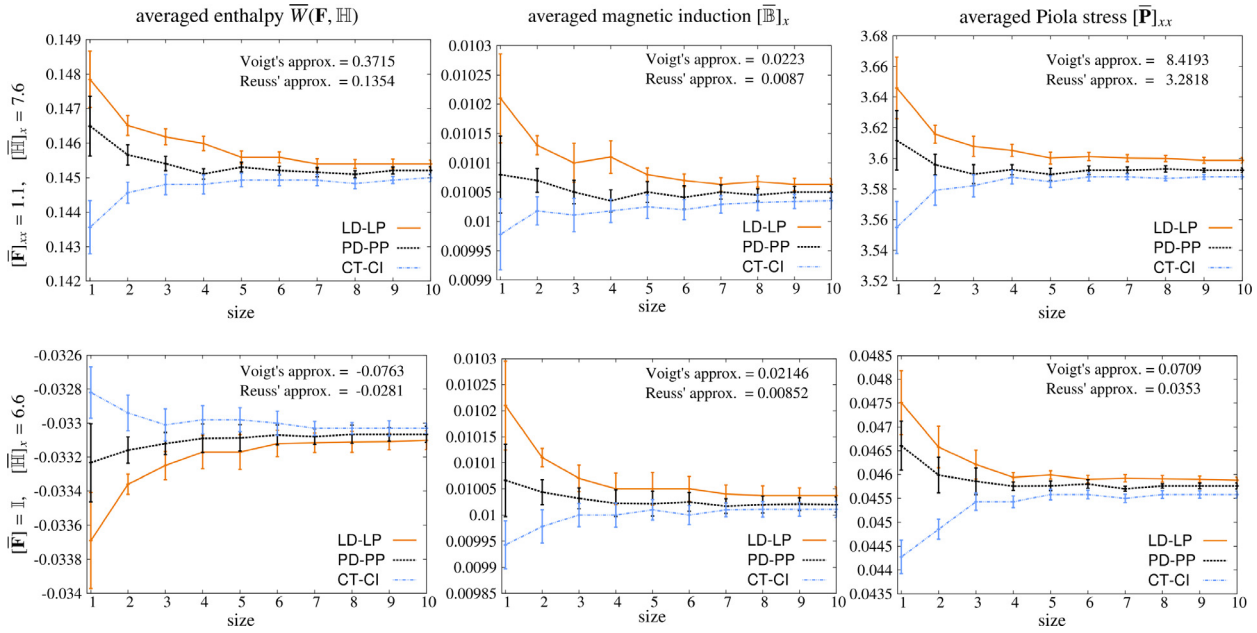

Fig. 13. Comparison of the macroscopic enthalpy $\overline{W}$, macroscopic magnetic induction $[\overline{\mathbb{B}}]_x$ and macroscopic Piola stress $[\overline{\mathbf{P}}]_{xx}$, obtained from the application of LD-LP, PD-PP, CT-CI b.cs. and Voigt's and Reuss' bounds to the random microstructures. The size of the RVE increases from a 1x1 to a 10x10 random poly-disperse microstructure that contains all underlying lower size RVEs. Macroscopic responses are obtained from the solution and averaging ten different random poly-disperse microstructures. The bars in the diagrams indicate the standard deviation of the results of poly-disperse microstructures from the average solution.

and Reuss' approximation a higher one. The reason for these unusual results is founded in the magneto-elastic enthalpy function itself, which is poly-convex in $\mathbf{F}$ (when $\mathbb{H}=0$) but concave in $\mathbb{H}$ in the magneto-mechanical case, compare Fig. (2). Therefore, the Voigt approximation does in general not result in the maximum magneto-elastic enthalpy values. This is not observed in the top row of Fig. 12, since that example is dominated by the mechanical response. Considering the stress, the results for both the LD-LP and the CT-CI boundary conditions approach the periodic result from below, whereby the LD-LP converge faster. This is due to the saddle-point structure of the enthalpy function together with the nonlinearity of the stress response.

It is analyzed in the next example if the same behavior can be observed for random poly-disperse microstructures. In Fig. 13 the homogenized magneto-elastic enthalpy, magnetic induction and stress are depicted for increasing sizes of random poly-disperse RVEs. The same load cases and boundary conditions as in the previous example are analyzed.

For the poly-disperse RVEs the periodic boundary conditions do not provide the exact solution and, therefore, the results of the periodic boundary conditions also change with an increasing size of the RVE. However, it can be observed in all cases, that they converge to a constant value (which is in general not the same as for the periodic microstructure). The results of the LD-LP and the CT-CI boundary conditions also converge to the periodic ones. The curves are not as smooth as in the example with the periodic microstructure which comes from the randomness of the particle distributions. Each curve represents the average values of 10 random poly-disperse RVEs of the same size. The error bars indicate the standard deviation, which decreases for the larger RVE sizes. Similar observations have been reported by Bayat and Gordaninejad (2017). They observed that for small RVE sizes the random positioning of inclusions has high influence on the effective responses. However, by increasing the RVE size and number of particles the oscillations and deviations of the effective responses significantly reduce. The order of the results for the different boundary conditions in Fig. 13 is similar as for the periodic microstructures. In the top row of Fig. 13 the magneto-mechanical load case is presented, where the mechanical loading dominates the problem and therefore the usual behavior is observed, i.e. Voigt's approximation gives the highest values, followed by the LD-LP, PD-PP and CT-CI boundary conditions, and Reuss' approximation results in the lowest values. For the poly-disperse RVEs the convergence rates of the LD-LP and CT-CI boundary conditions are similar. In the bottom row the results for magnetic loading with $\mathbf{F}=\mathbb{I}$ are depicted. Again, the saddle-point structure of the magneto-elastic enthalpy becomes apparent, since the Reuss' approximation gives the highest magneto-elastic enthalpy values, followed by the CT-CI, PD-PP and LD-LP boundary conditions and Voigt's approximation. For the magnetic induction and the stress LD-LP boundary conditions and Voigt's approximation overestimate the response while the CT-CI boundary conditions and Reuss' approximation underestimate them. The behavior of the stresses is different as compared to the periodic microstructure, since the LD-LP boundary conditions now approach the periodic ones from above as expected. This is not only observed for the average values but also for all random RVEs and therefore the observation made for periodic microstructures seems to be a peculiarity resulting from the regular microstructure.

It can be summarized for the random poly-disperse RVEs that the homogenized values obtained for different boundary conditions and various microstructures converge to certain similar values when the size of the RVE is increased. The maximum deviations occur in the RVE levels between 1×1 and 6×6 and the different curves start to show a more stable and smoother behavior for the RVE sizes above 7×7 cells. Periodic boundary conditions show as expected the fastest convergence to the homogenized values, whereas the convergence rates of the LD-LP and the CT-CI boundary conditions are similar.

The observations for the magneto-elastic enthalpy and the stresses in the purely magnetic load case for periodic and random microstructures show that it is not possible for the present setting of the coupled magneto-mechanical problem to ensure that e.g. Voigt's approximation or the LD-LP boundary conditions always overestimate the homogenized quantities as it holds for purely me-

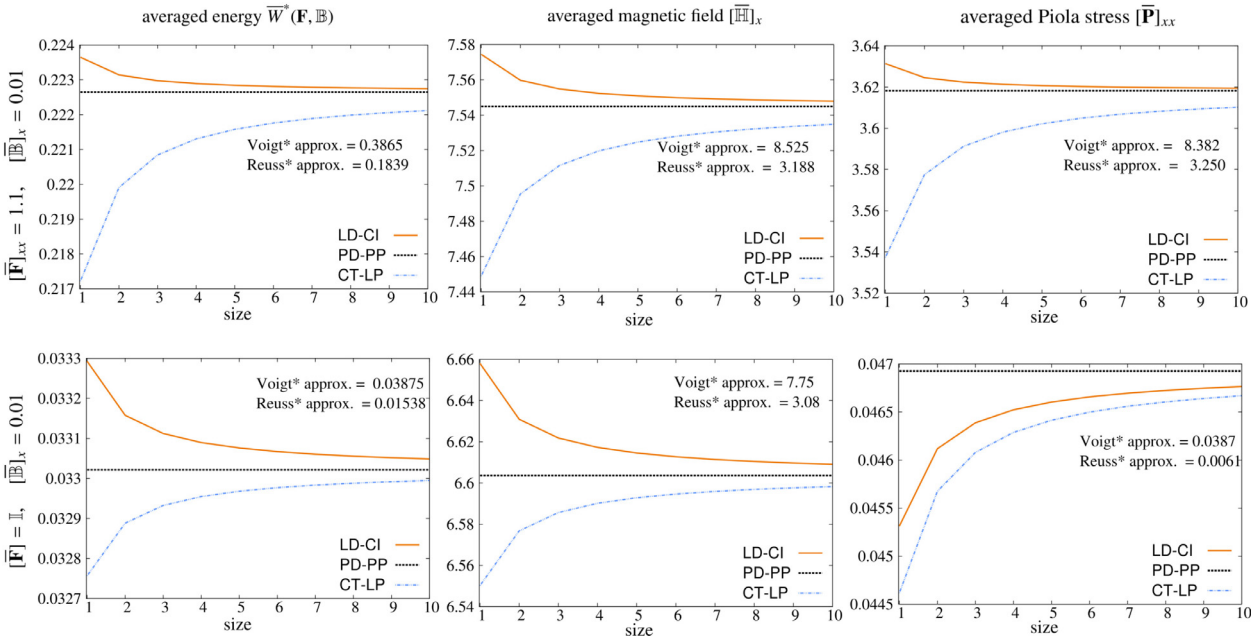

Fig. 14. Comparison of the macroscopic enthalpy $\overline{W}$, macroscopic magnetic induction $[\overline{\mathbb{B}}]_x$ and macroscopic Piola stress $[\overline{\mathbf{P}}]_{xx}$, obtained from the application of LD-CI, PD-PP, CT-LP b.cs. and Voigt* and Reuss* bounds to the periodic microstructures. The size of the RVE increases from a unit-cell to a 10x10 periodic microstructure that contains all underlying lower size RVEs.

chanical problems. This motivates the analysis of a second set of boundary conditions, formulated in the primary variables of the magneto-elastic internal energy function $W^*(\mathbf{F},\mathbb{B})$ which is poly-convex in $\mathbf{F}$ when $(\mathbb{B}=0)$ and convex in $\mathbb{B}$, in the next subsection.

3.3.2. Boundary conditions based on primary variables of energy function $W^*(\mathbf{F},\mathbb{B})$

In this subsection, boundary conditions formulated in $\mathbf{F}$ and $\mathbb{B}$, the primary variables of the magneto-elastic internal energy function W^* are applied, as introduced in Section 2.3. This is motivated by the fact that the magneto-elastic internal energy is poly-convex in $\mathbf{F}$ when $(\mathbb{B}=0)$ and convex in $\mathbb{B}$. Therefore, it is expected that the Voigt* and Reuss* approximations deliver bounds on the homogenized behavior. The following combinations of boundary conditions result: linear displacements and constant magnetic induction (LD-CI), periodic displacements and periodic magnetic potential (PD-PP) and constant tractions and linear magnetic potential (CT-LP). For Voigt* approximation, constant strains and a constant magnetic induction are assumed everywhere in the RVE, whereas Reuss* approximation prescribes constant stresses and a constant magnetic field in the RVE. Fig. 14 presents the evolution of the averaged magneto-elastic energy $\overline{W}^*$, the averaged magnetic field $[\overline{\mathbb{H}}]_x$ and the averaged Piola stress $[\overline{\mathbf{P}}]_{xx}$ versus the size of a periodic RVE. The composites undergo a magneto-mechanical load with $[\overline{\mathbf{F}}]_{xx}=1.1$ and $[\overline{\mathbb{B}}]_x=0.01$ (results in top row), and a magnetic load with $[\overline{\mathbf{F}}]=\mathbb{I}$ and $[\overline{\mathbb{B}}]_x=0.01$ (bottom row).

The upper plots of Fig. 14 show that the results of all boundary conditions lie between Voigt* and Reuss* approximations where the LD-CI b.c. overestimate the results of the periodic boundary conditions and the CT-LP b.c. yield lower averaged values than the other two boundary conditions. Furthermore, all results converge to the (constant) results related to the periodic boundary conditions, whereby convergence is faster for the LD-CI b.c. than for the CT-LP boundary conditions. For the second load case in the bottom row, a similar behavior is observed for the averaged magneto-elastic internal energy and the averaged magnetic field. Since the magneto-elastic internal energy $\overline{W}^*$ is poly-convex in $\mathbf{F}$ (when $\mathbb{B}=0$) and convex in $\mathbb{B}$, Voigt* and Reuss* assumptions deliver as expected the highest or lowest values, respectively. However, for the averaged stresses the Voigt* assumption does not render the maximum value since the deformation gradient is prescribed as $[\overline{\mathbf{F}}]=\mathbb{I}$ in the whole domain of $\mathcal{B}_0$ which cancels out the mechanical term of the Piola stress in Eq. (9). Furthermore, the results of both the LD-CI and the CT-LP boundary conditions approach the periodic ones from below. This behavior is again a consequence of the nonlinearity of the coupled constitutive relations and depends on the microstructure and the material parameters.

The homogenized magneto-elastic internal energy $\overline{W}^*$, the homogenized magnetic field $[\overline{\mathbb{H}}]_x$ and the homogenized Piola stress $[\overline{\mathbf{P}}]_{xx}$ for poly-disperse RVEs of different sizes are considered in Fig. 15. The error bars indicate again the standard deviations. The top row shows the results for the magneto-mechanical load case, the bottom row the results for the magnetic load case with $[\overline{\mathbf{F}}]=\mathbb{I}$. The three different boundary conditions are compared, complemented by the Voigt* and Reuss* approximations. Due to the randomness of the poly-disperse microstructure, the curves are not as smooth as in Fig. 14 for the periodic case, but the variations of the results and the convergence behavior are quite similar. Concerning the order of the results, all homogenized values, but the Piola stress in the second load case, show the highest values for the Voigt* approximation, followed by LD-CI, PD-PP, CT-LP and Reuss* approximation. For the Piola stress in the magnetic load case, the order is different and Voigt* approximation does not give the highest value.

To summarize the convergence analysis for the second set of boundary conditions, formulated in $\mathbf{F}$ and $\mathbb{B}$, it can be stated that as expected the results of all boundary conditions converge to the same homogenized quantities for an increasing size of RVEs. The Voigt* and Reuss* approximations yield bounds for the homogenized energy due to its convexity, but not for the homogenized Piola stress. This is due to the fact that the deformation gradient is prescribed as $[\overline{\mathbf{F}}]=\mathbb{I}$ in the whole domain of $\mathcal{B}_0$ which cancels out the mechanical term of the Piola stress in Eq. (9) and therefore the Voigt* assumption does not render the maximum value of the Piola stress.

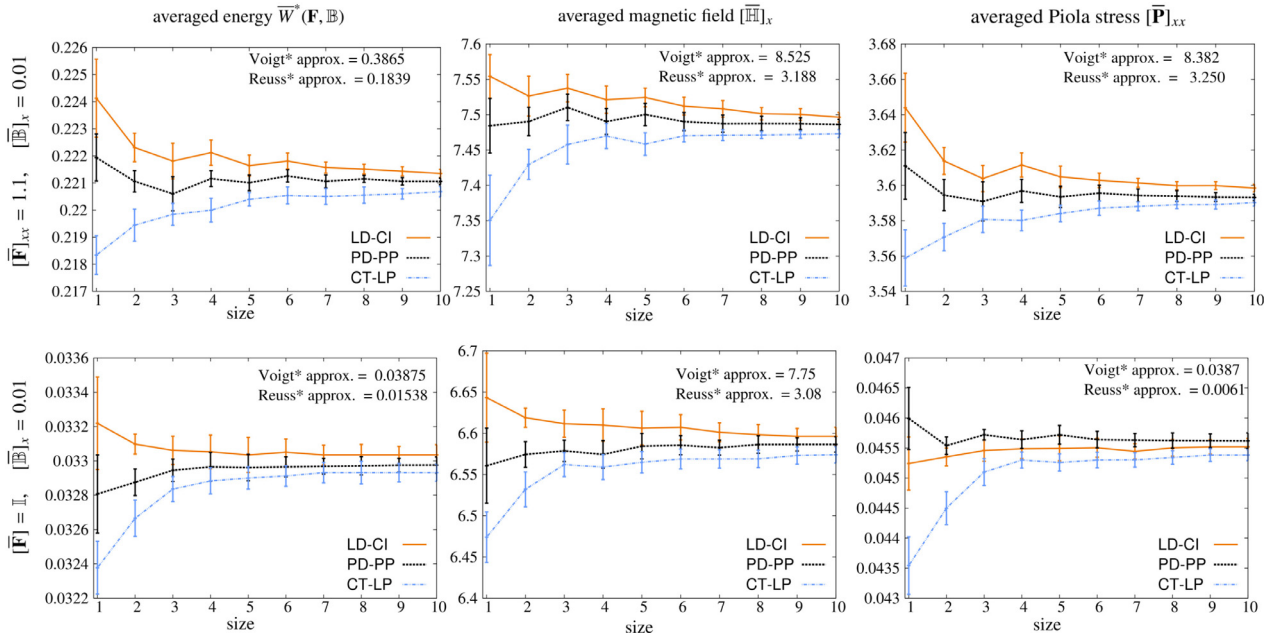

Fig. 15. Comparison of the macroscopic enthalpy $\overline{W}$, macroscopic magnetic induction $[\overline{\mathbb{B}}]_x$ and macroscopic Piola stress $[\overline{\mathbf{P}}]_{xx}$, obtained from the application of LD-CI, PD-PP, CT-LP b.cs. and Voigt* and Reuss* bounds to the random microstructures. The size of the RVE increases from a 1x1 to a 10x10 random poly-disperse microstructure that contains all underlying lower size RVEs. Macroscopic responses are obtained from the solution and averaging ten different random poly-disperse microstructures. The bars on the diagrams indicate the standard deviation of the results of poly-disperce microstructures from the average solution.

4. Conclusion

The behavior of heterogeneous magneto-rheological composites subjected to large deformations and external magnetic fields is studied. Computational homogenization is used to derive the macroscopic material response from the averaged response of the underlying microstructure. The microstructure consists of two materials and is far smaller than the characteristic length of the macroscopic problem. Different types of boundary conditions based on the primary variables of the magneto-elastic enthalpy and internal energy functionals are applied to solve the problem at the micro-scale. The overall responses of the RVEs with different sizes and particle distributions are studied under different loads and magnetic fields.

The finite element results indicate that the periodic RVEs represent a uniform microscopic response for the application of different boundary conditions and magneto-mechanical loads. However, the microscopic fields obtained from random microstructures show large variations and differ from the results of periodic RVEs. Thereby microscopic material behavior of a magneto-active composite strongly depends on the distribution of the particles and can be significantly different depending on the distances between the magnetic particles. Considering the modeling and simulation of magneto-active materials, it is very important to represent the microstructures as accurately as possible to compute the correct maximum values of stresses and magnetic inductions on the micro-scale.

A convergence study of the homogenized macroscopic fields for the boundary conditions based on the primary variables of the magneto-elastic enthalpy function $W(\mathbf{F},\mathbb{H})$ shows the dependency of the macroscopic results on the magneto-mechanical loading and the microstructure of the RVE. For instance, under purely magnetic loading Voigt's approximation renders the smallest enthalpy and Reuss' approximation the highest one. However, for the RVEs undergoing magneto-mechanical loads Voigt's and Reuss' approximations result in the expected highest and lowest macroscopic magneto-elastic enthalpy, respectively. The reason for these unusual results is founded in the magneto-elastic enthalpy function itself, which is poly-convex in $\mathbf{F}$ (when $\mathbb{H}=0$) but concave in $\mathbb{H}$ in the magneto-mechanical case. The same study is carried out for the boundary conditions based on the magneto-elastic internal energy function $W^*(\mathbf{F},\mathbb{B})$. The results represent a consistent response of the homogenized fields for different magneto-elastic loadings and microstructures. Since the magneto-elastic energy $W^*(\mathbf{F},\mathbb{B})$ is poly-convex in $\mathbf{F}$ (when $\mathbb{B}=0$) and convex in $\mathbb{B}$, Voigt* and Reuss* assumptions always deliver the highest and the lowest values of the homogenized energy as expected, respectively. However, this result can not be transferred to the stresses, which show the highest values for the periodic boundary condition.

Furthermore, increasing the sizes of the RVEs, the homogenized responses obtained from non-periodic boundary conditions based on $W(\mathbf{F},\mathbb{H})$ and $W^*(\mathbf{F},\mathbb{B})$ converge to the results associated with periodic boundary conditions. However, for the poly-disperse random microstructures the convergence behavior is not as smooth as the behavior when the particles are uniformly distributed. It is also observed that the larger the size of the RVE (bigger than 7x7 in our study), the smoother the oscillatory response of the random microstructures.

Acknowledgments

The support of this work by the ERC Advanced Grant MOCOPOLY is gratefully acknowledged.

Appendix A. Numerical implementation

In the appendix the FE-formulation and numerical implementation of the homogenization problem are presented. Initially the FE-formulation for solving the magneto-mechanical homogenization problem is given and afterwards the algorithms for the implementation of various types of mixed boundary conditions are discussed.

A1. Finite element discretization

In the absence of microscopic inertia and mechanical body forces, the weak form of the microscopic equilibrium equation in the material configuration (2) is written as

$$\int_{\mathcal{B}_0} \mathbf{P} : \nabla_{\mathbf{X}}\, \delta\boldsymbol{\phi}\; \mathrm{d}V - \int_{\partial\mathcal{B}_0{}^{\mathcal{N}_{mech}}} \delta\boldsymbol{\phi}\cdot\mathbf{T}^p\; \mathrm{d}A = 0 \qquad \forall\delta\boldsymbol{\phi} \in \mathcal{H}_0{}^1(\mathcal{B}_0). \tag{A.1}$$

In a near-identical fashion, the weak form of the magneto-static problem can be derived by testing the local conservation of magnetic flux (4) with a scalar test function $\delta\varphi \in \mathcal{H}_0^1(\mathcal{B}_0)$ and then integrating the result over the corresponding domain in the material configuration. The global weak form of the magnetic balance equation reads

$$\int_{\mathcal{B}_0} \mathbb{B}\cdot\nabla_{\mathbf{X}}\, \delta\varphi\; \mathrm{d}V - \int_{\partial\mathcal{B}_0{}^{\mathcal{N}_{mag}}} \delta\varphi\; \mathbb{T}^p\; \mathrm{d}A = 0 \qquad \forall\delta\varphi \in \mathcal{H}_0{}^1(\mathcal{B}_0). \tag{A.2}$$

The geometry of the problem is discretized with finite elements and the unknown field values are approximated by means of element-wise polynomial shape functions. The spatial discretization of the problem domain is performed using the Bubnov–Galerkin finite element method. The geometry of the body in the reference configuration $\mathcal{B}_0$ is subdivided into a set of elements

$$\mathcal{B}_0{}^h \approx \bigcup_{\beta=1}^{\mathrm{nel}} \mathcal{B}_0{}^\beta$$

where nel denotes the number of elements. The geometry, the deformation and the magnetic potential (and their test functions) are approximated element-wise with the shape functions N^i and nodal values $(\bullet)^i$ at the nN element nodes.

$$\mathbf{X}\Big|_{\mathcal{B}_0{}^\beta} \approx \mathbf{X}^h = \sum_{i=1}^{nN} N^i\mathbf{X}^i\,, \qquad \boldsymbol{\phi}\Big|_{\mathcal{B}_0{}^\beta} \approx \boldsymbol{\phi}^h = \sum_{i=1}^{nN} N^i\boldsymbol{\phi}^i\,,$$
$$\varphi\Big|_{\mathcal{B}_0{}^\beta} \approx \varphi^h = \sum_{i=1}^{nN} N^i\varphi^i\,. \tag{A.3}$$

The discrete forms of the balance equations are obtained by inserting the approximations (A.3) into the weak forms (A.1) and (A.2) and result in the mechanical and magnetic residuals associated with the global node I

$$\mathbf{R}^I_{\boldsymbol{\phi}} := \mathop{\mathsf{A}}_{\beta=1}^{\mathrm{nel}}\left[\int_{\mathcal{B}_0{}^\beta} \mathbf{P}\cdot\nabla_{\mathbf{X}}\, N^i\,\mathrm{d}V - \int_{\partial\mathcal{B}_0{}^{\beta\mathcal{N}_{mech}}} \mathbf{T}^p\; N^i\,\mathrm{d}A\right] = \mathbf{0},$$
$$\mathrm{R}^I_{\varphi} := \mathop{\mathsf{A}}_{\beta=1}^{\mathrm{nel}}\left[\int_{\mathcal{B}_0{}^\beta} \mathbb{B}\cdot\nabla_{\mathbf{X}}\, N^i\,\mathrm{d}V - \int_{\partial\mathcal{B}_0{}^{\beta\mathcal{N}_{mag}}} \mathbb{T}^p\; N^i\,\mathrm{d}A\right] = 0.$$

This global system of equations is solved using the Newton–Raphson scheme. For further details regarding the discretization see Javili et al. (2013a).

A2. Boundary conditions

In this section various algorithms to apply the boundary conditions specified in Table 1 are discussed in detail. We focus on the two categories based on either prescribing $(\overline{\mathbf{F}}, \overline{\mathbb{H}})$ (i.e. the primary variables of the magneto-elastic enthalpy function) or prescribing $(\overline{\mathbf{F}}, \overline{\mathbb{B}})$ (i.e. the primary variables of the magneto-elastic energy function), respectively. For boundary conditions based on $(\overline{\mathbf{F}}, \overline{\mathbb{H}})$ we assume that the macroscopic input consists of $\overline{\mathbf{F}}$ and $\overline{\mathbb{H}}$ and for the second set of boundary conditions based on $(\overline{\mathbf{F}}, \overline{\mathbb{B}})$ the macroscopic variables $\overline{\mathbf{F}}$ and $\overline{\mathbb{B}}$ are the input variables. However, the algorithms could be easily adapted to other macroscopic input parameters.

A2.1. Boundary conditions based on prescribed $(\overline{\mathbf{F}}, \overline{\mathbb{H}})$

LD-LP boundary condition: The deformation and the magnetic potential of the boundary nodes are prescribed using the input values of the macroscopic deformation gradient $\overline{\mathbf{F}}$ and the macroscopic magnetic field $\overline{\mathbb{H}}$. The algorithm to implement LD-LP b.c. is given in the Algorithm 1 [4]:

Algorithm 1: Linear displacement-linear magnetic potential boundary condition b.c.

input: $\overline{\mathbf{F}}$ and $\overline{\mathbb{H}}$
prescribe $\boldsymbol{\phi}^i = \overline{\mathbf{F}}\cdot\mathbf{X}^i$ and $\varphi^i = \overline{\mathbb{H}}\cdot\mathbf{X}^i$ to the boundary nodes
solve the nonlinear system of equations (A.4) and (A.5) using the Newton-Raphson method
compute the macroscopic stress $\overline{\mathbf{P}} = \langle\mathbf{P}\rangle$ and magnetic induction $\overline{\mathbb{B}} = \langle\mathbb{B}\rangle$.

PD-PP boundary condition: The boundary of the RVE is decomposed into positive, $\partial\mathcal{B}_0{}^+$, and negative, $\partial\mathcal{B}_0{}^-$, parts with $\partial\mathcal{B}_0{}^+ \cup \partial\mathcal{B}_0{}^- = \partial\mathcal{B}_0$ and $\partial\mathcal{B}_0{}^+ \cap \partial\mathcal{B}_0{}^- = \{\emptyset\}$. Periodic boundary conditions require the equivalence of the micro-fluctuation fields on each opposite pair of boundary nodes, $\widetilde{\boldsymbol{\phi}}^{i+} = \widetilde{\boldsymbol{\phi}}^{i-}$ and $\widetilde{\varphi}^{i+} = \widetilde{\varphi}^{i-}$, which can be written in general format as

$$\boldsymbol{\phi}^{i+} - \boldsymbol{\phi}^{i-} = \overline{\mathbf{F}}\cdot[\mathbf{X}^{i+} - \mathbf{X}^{i-}] \quad \text{and} \quad \varphi^{i+} - \varphi^{i-} = \overline{\mathbb{H}}\cdot[\mathbf{X}^{i+} - \mathbf{X}^{i-}]\,. \tag{A.6}$$

Moreover, on each opposite part of the RVE boundary, the normal vectors are $\mathbf{N}^+ = -\mathbf{N}^-$. Therefore, the tractions and magnetic fluxes are anti-periodic at corresponding points on $\partial\mathcal{B}_0{}^+$ and $\partial\mathcal{B}_0{}^-$,

$$\mathbf{T}^+ = -\mathbf{T}^- \quad \text{and} \quad \mathbb{T}^+ = -\mathbb{T}^-. \tag{A.7}$$

The implementation of the periodic boundary condition is given in Algorithm 2 , see Tyrus et al. (2007) and Kouznetsova et al. (2001) for further details.

Algorithm 2: Periodic displacements-periodic magnetic potential b.c.

input: $\overline{\mathbf{F}}$ and $\overline{\mathbb{H}}$
prescribe $\boldsymbol{\phi}^i = \overline{\mathbf{F}}\cdot\mathbf{X}^i$ and $\varphi^i = \overline{\mathbb{H}}\cdot\mathbf{X}^i$ to the corner nodes
prescribe $\boldsymbol{\phi}^{i+} = \overline{\mathbf{F}}\cdot[\mathbf{X}^{i+} - \mathbf{X}^{i-}] + \boldsymbol{\phi}^{i-}$ and $\varphi^{i+} = \overline{\mathbb{H}}\cdot[\mathbf{X}^{i+} - \mathbf{X}^{i-}] + \varphi^{i-}$ on the boundary nodes at $\partial\mathcal{B}_0{}^+$ (using static condensation)
solve the nonlinear system of equations (A.4) and (A.5) using the Newton-Raphson method
compute the macroscopic stress $\overline{\mathbf{P}} = \langle\mathbf{P}\rangle$ and magnetic induction $\overline{\mathbb{B}} = \langle\mathbb{B}\rangle$.

CT-CI boundary condition: The application of CT-CI boundary conditions follows an algorithm introduced in Javili et al. (2017). It is based on the idea that the rigid body rotation of the RVE has to be constrained in such a manner that no additional stresses result due to these constraints. In the present two-dimensional setting, one corner of the RVE is fixed to prohibit rigid body translation, point I in Fig. A.16. Another degree of freedom at a second corner of the RVE, point II in Fig. A.16, has to be prescribed as a still unknown value d to avoid rigid body rotation. The unknown value

[4] $\langle\{\bullet\}\rangle = \frac{1}{V_0}\int_{\mathcal{B}_0}\{\bullet\}\,dV$ denotes averaging over the RVE.

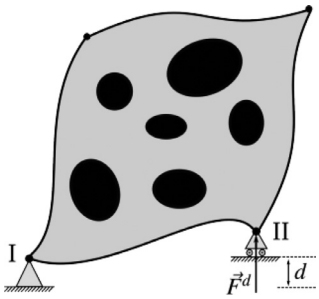

Fig. A.16. Representative volume element for CT-CI boundary condition.

d follows from the requirement that the additionally introduced stress $\mathbf{P}^d$ due to this constraint has to vanish.

To apply the CT-CI boundary conditions (for prescribed macroscopic deformation gradient $\overline{\mathbf{F}}$ and magnetic induction $\overline{\mathbb{H}}$), initial values for the constant traction and the constant magnetic flux are applied to the RVE's boundary. The boundary value problem is solved and the resulting averaged deformation gradient and magnetic induction are compared with their macroscopic input values. Additionally, the stress $\mathbf{P}^d$ due to the artificial constraint has to vanish. Therefore, the constant traction and the constant magnetic flux on the boundary are incrementally updated until the following error E vanishes

$$E = \|\overline{\mathbf{F}} - \langle \mathbf{F} \rangle\| + \|\overline{\mathbb{H}} - \langle \mathbb{H} \rangle\| + \|\mathbf{P}^d\| = 0\,. \tag{A.8}$$

The implementation of the constant traction-constant magnetic field boundary condition is given in the Algorithm 3.

Algorithm 3: Constant traction-constant magnetic induction b.c.

input: $\overline{\mathbf{F}}$ and $\overline{\mathbb{H}}$
initialize $\overline{\mathbf{P}}$ and $\overline{\mathbb{B}}$
while $E > tol$ **do**
  apply $\overline{\mathbf{T}} = \overline{\mathbf{P}} \cdot \mathbf{N}$ and $\overline{\mathbb{T}} = \overline{\mathbb{B}} \cdot \mathbf{N}$ to the boundary nodes
  fix corner nodes I,II (Fig. A.16)
  solve the nonlinear system of equations (A.4) and (A.5) using the Newton-Raphson method
  compute E
  update $\overline{\mathbf{P}}, \overline{\mathbb{B}}, d$
end

Voigt's and Reuss' assumptions: Voigt's assumption is an approximate solution which assumes that the deformation gradient $\overline{\mathbf{F}}$ and the magnetic field $\overline{\mathbb{H}}$ are constant throughout the whole domain. In other words, the inclusion and the matrix undergo the same linear mapping and magnetic potential. Therefore, the Piola stress and the magnetic induction can be obtained directly from Eqs. (9) and (11) for the matrix and inclusion materials, individually. The total macroscopic variables are then calculated as the weighted average of their counterparts in matrix and inclusion

$$\begin{aligned} \langle \mathbf{P} \rangle &= f\,\mathbf{P}^{inc.} + [1-f]\,\mathbf{P}^{mat.} \quad \text{and} \\ \langle \mathbb{B} \rangle &= f\,\mathbb{B}^{inc.} + [1-f]\,\mathbb{B}^{mat.} \quad \text{with } f \text{ being the volume fraction of the inclusion.} \end{aligned} \tag{A.9}$$

Reuss' approximation assumes a uniform stress and magnetic induction throughout the RVE domain. Since Eqs. (9) and (11) can not easily be inverted, the Reuss' approximation is computed iteratively. Initial value for the stress and the magnetic induction are prescribed for the matrix and the inclusion. These values are iteratively updated until the resulting averaged deformation gradient and the averaged magnetic field

$$\begin{aligned} \langle \mathbf{F} \rangle &= f\,\mathbf{F}^{inc.} + [1-f]\,\mathbf{F}^{mat.}, \\ \langle \mathbb{H} \rangle &= f\,\mathbb{H}^{inc.} + [1-f]\,\mathbb{H}^{mat.} \end{aligned} \tag{A.10}$$

are equal to the macroscopic input parameters $\overline{\mathbf{F}}$ and $\overline{\mathbb{H}}$.

A.2.2. Algorithms for boundary value problems based on prescribed $(\overline{\mathbf{F}}, \overline{\mathbb{B}})$

LD-CI boundary condition: Using the input parameters $\overline{\mathbf{F}}$ and $\overline{\mathbb{B}}$, the deformation and the magnetic induction are imposed on the boundary nodes. The algorithm to implement LD-CI b.c. is given in the Algorithm 4.

Algorithm 4: Linear displacement-constant magnetic induction b.c.

input: $\overline{\mathbf{F}}$ and $\overline{\mathbb{B}}$
prescribe $\boldsymbol{\phi}^i = \overline{\mathbf{F}} \cdot \mathbf{X}^i$ and $\overline{\mathbb{T}} = \overline{\mathbb{B}} \cdot \mathbf{N}$ to the boundary nodes
solve the nonlinear system of equations (A.4) and (A.5) using the Newton–Raphson method
compute the macroscopic stress $\overline{\mathbf{P}} = \langle \mathbf{P} \rangle$ and magnetic field $\overline{\mathbb{H}} = \langle \mathbb{H} \rangle$.

PD-PP boundary condition: Essentially, the implementation of the PD-PP b.c. based on the primary variables of the magneto-elastic internal energy function is similar to the one based on the primary variables of the magneto-elastic enthalpy function, see Algorithm 2. However, here the input parameters are the macroscopic deformation gradient $\overline{\mathbf{F}}$ and the macroscopic induction $\overline{\mathbb{B}}$. Therefore, the algorithm is equipped with an extra iteration loop which ensures that the macroscopic induction is equal to the averaged one. The deformation gradient and initial magnetic field are prescribed to the boundary nodes. In the next step, the initial $\overline{\mathbb{H}}$ has to be updated incrementally until the average of the magnetic induction $\langle \mathbb{B} \rangle$ is equivalent to the macroscopic induction $\overline{\mathbb{B}}$. This procedure is done by the minimization of the following error E

$$E = \|\overline{\mathbb{B}} - \langle \mathbb{B} \rangle\| = 0\,. \tag{A.11}$$

The implementation of the periodic boundary condition is given in Algorithm 5.

Algorithm 5: Periodic displacements-periodic magnetic potential b.c.

input: $\overline{\mathbf{F}}$ and $\overline{\mathbb{B}}$
initialize $\overline{\mathbb{H}}$
while $E > tol$ **do**
  prescribe $\boldsymbol{\phi}^i = \overline{\mathbf{F}} \cdot \mathbf{X}^i$ and $\varphi^i = \overline{\mathbb{H}} \cdot \mathbf{X}^i$ to the corner nodes
  prescribe $\boldsymbol{\phi}^{i+} = \overline{\mathbf{F}} \cdot [\mathbf{X}^{i+} - \mathbf{X}^{i-}] + \boldsymbol{\phi}^{i-}$,
  $\varphi^{i+} = \overline{\mathbb{H}} \cdot [\mathbf{X}^{i+} - \mathbf{X}^{i-}] + \varphi^{i-}$ on the boundary nodes at $\partial \mathcal{B}_0{}^+$
  solve the nonlinear system of equations (A.4) and (A.5) using the Newton–Raphson method
  compute E
  update $\overline{\mathbb{H}}$
end
compute the macroscopic stress $\overline{\mathbf{P}} = \langle \mathbf{P} \rangle$.

CT-LP boundary condition: An initial traction $\overline{\mathbf{T}} = \overline{\mathbf{P}} \cdot \mathbf{N}$ and magnetic field $\overline{\mathbb{H}}$ are imposed to the boundary nodes. Similar to the CT-CI condition, an initial displacement d is applied to a corner node to prevent rigid body motion. In the next step, the prescribed $\overline{\mathbf{P}}$, $\overline{\mathbb{H}}$ and d have to be updated iteratively until the averaged deformation gradient $\langle \mathbf{F} \rangle$ and magnetic induction $\langle \mathbb{B} \rangle$ are equal to their

macroscopic counterparts $\overline{\mathbf{F}}$ and $\overline{\mathbb{B}}$ and the artificial stress $\mathbf{P}^d$ vanishes. The following error E is iteratively minimized

$$E = \|\overline{\mathbf{F}} - \langle \mathbf{F} \rangle\| + \|\overline{\mathbb{B}} - \langle \mathbb{B} \rangle\| + \|\mathbf{P}^d\| = 0. \tag{A.12}$$

The implementation of the constant traction-linear magnetic potential boundary condition is given in Algorithm 6.

Algorithm 6: Constant traction-linear magnetic potential b.c.

```
input: F̄ and B̄
initialize P̄, H̄
while E > tol do
    apply T̄ = P̄ · N and φ^i = H̄ · X^i to the boundary nodes
    fix corner nodes I,II (Fig. A.16)
    solve the nonlinear system of equations (A.4) and (A.5)
    using the Newton–Raphson method
    compute E
    update P̄, H̄, d
end
```

Voigt* and Reuss* assumptions: In Voigt* assumption $\overline{\mathbf{F}}$ and $\overline{\mathbb{B}}$ are prescribed to be constant in $\mathcal{B}_0$. The Piola stress and the magnetic field are obtained directly from the Eqs. (13) and (14) for the matrix and inclusion materials, individually. The averaged (macroscopic) variables are then calculated as the weighted average of their counterparts in matrix and inclusion

$$\begin{aligned} \langle \mathbf{P} \rangle &= f\, \mathbf{P}^{inc.} + [1-f]\, \mathbf{P}^{mat.}, \\ \langle \mathbb{H} \rangle &= f\, \mathbb{H}^{inc.} + [1-f]\, \mathbb{H}^{mat.}. \end{aligned} \tag{A.13}$$

In the Reuss* assumption, $\mathbf{P}$ and $\mathbb{H}$ are constant in $\mathcal{B}_0$ such that $\langle \mathbf{F} \rangle$ and $\langle \mathbb{B} \rangle$ are equal to their macroscopic counterparts. Therefore, Eqs. (13) and (14) have to be solved iteratively for the unknown $\mathbb{B}^{mat.}$, $\mathbb{B}^{inc.}$, $\mathbf{F}^{mat.}$ and $\mathbf{F}^{inc.}$ until

$$\begin{aligned} \overline{\mathbf{F}} = \langle \mathbf{F} \rangle &= f\, \mathbf{F}^{inc.} + [1-f]\, \mathbf{F}^{mat.}, \\ \overline{\mathbb{B}} = \langle \mathbb{B} \rangle &= f\, \mathbb{B}^{inc.} + [1-f]\, \mathbb{B}^{mat.}. \end{aligned} \tag{A.14}$$

References

Bayat, A., Gordaninejad, F., 2017. Characteristic volume element for randomly particulate magnetoactive composites. ASME J. Eng. Mater.Technol. 140. 011003-011003-10

Belytschko, T., Liu, W.K., Moran, B., Elkhodary, K., 2013. Nonlinear Finite Elements for Continua and Structures, 2nd edition wiley.

Borcea, L., Bruno, O., 2001. On the magneto-elastic properties of elastomer-ferromagnet composites. J. Mech. Phys. Solids 49, 2877–2919.

Brigadnov, I.A., Dorfmann, A., 2003. Mathematical modeling of magneto-sensitive elastomers. Int. J. Solids Struct. 40, 4659–4674.

Bustamante, R., Dorfmann, A., Ogden, R.W., 2008. On variational formulations in nonlinear magnetoelastostatics. Math. Mech. Solids 13, 725–745.

Bustamante, R., Dorfmann, A., Ogden, R.W., 2011. Numerical solution of finite geometry boundary-value problems in nonlinear magnetoelasticity. Int. J. Solids Struct. 48 (6), 874–883.

Carlson, J.D., Jolly, M.R., 2000. MR fluid, foam and elastomer devices. Mechatronics 10, 555–569.

Castañeda, P.P., Galipeau, E., 2011. Homogenization-based constitutive models for magnetorheological elastomers at finite strain. J. Mech. Phys. Solids 59 (2), 194–215.

Castañeda, P.P., Siboni, M.H., 2012. A finite-strain constitutive theory for electro-active polymer composites via homogenization. Int. J. Non Linear Mech. 47 (2), 293–306.

Chatzigeorgiou, G., Javili, A., Steinmann, P., 2014. Unified magnetomechanical homogenization framework with application to magnetorheological elastomers. Math. Mech. Solids 19 (2), 193–211.

Costanzo, F., Gray, G.L., Andia, P.C., 2005. On the definitions of effective stress and deformation gradient for use in MD: Hill's macro-homogeneity and the virial theorem. Int. J. Eng. Sci. 43 (7), 533–555.

Danas, K., 2017. Effective response of classical, auxetic and chiral magnetoelastic materials by use of a new variational principle. J. Mech. Phys. Solids 105, 25–53.

Danas, K., Kankanala, S.V., Triantafyllidis, N., 2012. Experiments and modeling of iron-particle-filled magnetorheological elastomers. J. Mech. Phys. Solids 60 (1), 120–138.

Doll, S., Schweizerhof, K., 1999. On the development of volumetric strain energy functions. ASME J. Appl. Mech. 67 (1), 17–21.

Dorfmann, A., Ogden, R.W., 2004. Nonlinear magnetoelastic deformations on elastomers. Acta Mech. 167 (1–2), 13–28.

Galipeau, E., Ponte Castañeda, P., 2013. A finite-strain constitutive model for magnetorheological elastomers: magnetic torques and fiber rotations. J. Mech. Phys. Solids 61 (4), 1065–1090.

Gil, A.J., Ortigosa, R., 2016. A new framework for large strain electromechanics based on convex multi-variable strain energies: variational formulation and material characterisation. Comput. Methods Appl. Mech. Eng. 302, 293–328.

Hill, R., 1963. Elastic properties of reinforced solids: some theoretical principles. J. Mech. Phys. Solids 11, 357–372.

Hill, R., Rice, J., 1972. Constitutive analysis of elastic-plastic crystals at arbitrary strain. J. Mech. Phys. Solids 20 (6), 401–413.

Hirschberger, C.B., Sukumar, N., Steinmann, P., 2008. Computational homogenization of material layers with micromorphic mesostructure. Philos. Mag. 88 (30–32), 3603–3631.

Javili, A., Chatzigeorgiou, G., Steinmann, P., 2013. Computational homogenization in magneto-mechanics. Int. J. Solids Struct. 50 (25–26), 4197–4216.

Javili, A., McBride, A., Mergheim, J., Steinmann, P., Schmidt, U., 2013. Micro-to-macro transitions for continua with surface structure at the microscale. Int. J. Solids Struct. 50 (16–17), 2561–2572.

Javili, A., Saeb, S., Steinmann, P., 2017. Aspects of implementing constant traction boundary conditions in computational homogenization via semi-dirichlet boundary conditions. Comput. Mech. 59 (1), 21–35.

Jolly, M.R., Carlson, J.D., Munoz, B.C., 1996. A model of the behavior of magneto-rheological materials. Smart Mater. Struct. 5, 607–614.

Kankanala, S.V., Triantafyllidis, N., 2004. On finitely strained magnetorheological elastomers. J. Mech. Phys. Solids 52, 2869–2908.

Keip, M., Rambausek, M., 2016. A multiscale approach to the computational characterization of magnetorheological elastomers. Int. J. Numer. Methods Eng. 107 (4), 338–360.

Keip, M.A., Steinmann, P., Schröder, J., 2014. Two-scale computational homogenization of electro-elasticity at finite strains. Comput. Methods Appl. Mech. Eng. 278, 62–79.

Kordonsky, W., 1993. Magneto-rheological effects as a base of new devices and technologies. J. Magn. Magn. Mater. 122, 395–398.

Kouznetsova, V., Brekelmans, W.A.M., Baaijens, F.P.T., 2001. An approach to micro–macro modeling of heterogeneous materials. Comput. Mech. 27 (1), 37–48.

Kouznetsova, V., Geers, M.G.D., Brekelmans, W.A.M., 2002. Multi-scale constitutive modelling of heterogeneous materials with a gradient-enhanced computational homogenization scheme. Int. J. Numer. Methods Eng. 54 (8), 1235–1260.

Kovetz, A., 2000. Electromagnetic Theory. Oxford, New York.

Kuznetsov, S., Fish, J., 2012. Mathematical homogenization theory for electroactive continuum. Int. J. Numer. Methods Eng. 91 (11), 1199–1226.

Matous, K., Geers, M.G.D., Kouznetsova, V.G., Gillman, A., 2017. A review of predictive nonlinear theories for multiscale modeling of heterogeneous materials. J. Comput. Phys. 330, 192–220.

Miehe, C., Koch, A., 2002. Computational micro-to-macro transitions of discretized microstructures undergoing small strains. Arch. Appl. Mech. 72 (4–5), 300–317.

Miehe, C., Schröder, J., Schotte, J., 1999. Computational homogenization analysis in finite plasticity simulation of texture development in polycrystalline materials. Comput. Methods Appl. Mech. Eng. 171 (3–4), 387–418.

Miehe, C., Vallicotti, D., Teichtmeister, S., 2016. Homogenization and multiscale stability analysis in finite magneto-electro-elasticity. application to soft matter EE, ME and MEE composites. Comput. Methods Appl. Mech. Eng. 300, 294–346.

Ortigosa, R., Gil, A.J., 2016. A new framework for large strain electromechanics based on convex multi-variable strain energies: conservation laws, hyperbolicity and extension to electro-magneto-mechanics. Comput. Methods Appl. Mech. Eng. 202–242 (309).

Ortigosa, R., Gil, A.J., 2016. A new framework for large strain electromechanics based on convex multi-variable strain energies: finite element discretisation and computational implementation. Comput. Methods Appl. Mech. Eng. 302, 329–360.

Ortigosa, R., Gil, A.J., 2017. A computational framework for incompressible electromechanics based on convex multi-variable strain energies for geometrically exact shell theory. Comput. Methods Appl. Mech. Eng. 317, 792–816.

Ortigosa, R., Gil, A.J., Chun Hean, L., 2016. A computational framework for large strain nearly and truly incompressible electromechanics based on convex multi-variable strain energies. Comput. Methods Appl. Mech. Eng. 310, 297–334.

Özdemir, I., Brekelmans, W.A.M., Geers, M.G.D., 2008. Computational homogenization for heat conduction in heterogeneous solids. Int. J. Numer. Methods Eng. 73 (2), 185–204. ISSN 1097-0207

Pindera, M.J., Khatam, H., Drago, A.S., Bansal, Y., 2009. Micromechanics of spatially uniform heterogeneous media: a critical review and emerging approaches. Compos. Part B 40 (5), 349–378.

Ponte Castañeda, P., 1996. Exact second-order estimates for the effective mechanical properties of nonlinear composite materials. J. Mech. Phys. Solids 44 (6), 827–862.

Ponte Castañeda, P., Galipeau, E., 2011. Homogenization-based constitutive models for magneto-rheological elastomers at finite strain. J. Mech. Phys. Solids 59 (2), 194–215.

Saeb, S., Steinmann, P., Javili, A., 2016. Aspects of computational homogenization at finite deformations: a unifying review from reuss' to voigt's bound. Appl. Mech. Rev. 68 (5), 050801.

Schröder, J., Keip, M.A., 2012. Two-scale homogenization of electromechanically coupled boundary value problems. Comput. Mech. 50 (2), 229–244.

Sridhar, A., Keip, M.-A., Miehe, C., 2016. Homogenization in micro-magneto-mechanics. Comput. Mech. 58 (1), 151–169.

Steigmann, D.J., 2004. Equilibrium theory for magnetic elastomers and magnetoelastic membranes. Int. J. Non Linear Mech. 39, 1193–1216.
Temizer, I., Wriggers, P., 2008. On the computation of the macroscopic tangent for multiscale volumetric homogenization problems. Comput. Methods Appl. Mech. Eng. 198 (3–4), 495–510.
Temizer, I., Wriggers, P., 2011. Homogenization in finite thermoelasticity. J. Mech. Phys. Solids 59, 344–372. 2
Terada, K., Kikuchi, N., 1995. Nonlinear homogenization method for practical applications. ASME Appl.Mech.Div.Publ.-AMD 212, 1–16.
Terada, K., Kikuchi, N., 2001. A class of general algorithms for multi-scale analyses of heterogeneous media. Comput. Methods Appl. Mech. Eng. 190, 5427–5464.
Tyrus, J.M., Gosz, M., DeSantiago., E., 2007. A local finite element implementation for imposing periodic boundary conditions on composite micromechanical models. Int. J. Solids Struct. 44 (9), 2972–2989.
Vu, D.K., Steinmann, P., 2007. Nonlinear electro- and magneto-elastostatics: material and spatial settings. Int. J. Solids Struct. 44, 7891–7905.
Vu, D.K., Steinmann, P., 2010. Material and spatial motion problems in nonlinear electro- and magneto-elastostatics. Math. Mech. Solids 15 (2), 239–257.
Wang, J.S., Chen, D., Sun, L., 2003. Homogenization of magnetostrictive particle-filled elastomers using an interface-enriched reproducing kernel particle method. Finite Elem. Anal. Des. 39 (8), 765–782.
Yin, H.M., Sun, L.Z., Chen, J.S., 2002. Micromechanics-based hyperelastic constitutive modeling of magnetostrictive particle-filled elastomers. Mech. Mater. 34, 505–516.
Yin, H.M., Sun, L.Z., Chen, J.S., 2006. Magneto-elastic modeling of composites containing chain-structured magnetostrictive particles. J. Mech. Phys. Solids 54, 975–1003.
Yvonnet, J., Gonzalez, D., He, Q.C., 2009. Numerically explicit potentials for the homogenization of nonlinear elastic heterogeneous materials. Comput. Methods Appl. Mech. Eng. 198 (33–36), 2723–2737.
Zohdi, T.I., Wriggers, P., 2001. Computational micro-macro material testing. Arch. Comput. Methods Eng. 8 (2), 131–228.